Research Square

Preprints are preliminary reports that have not undergone peer review.
They should not be considered conclusive, used to inform clinical practice,
or referenced by the media as validated information.

Composition-Driven Defect and Interface Engineering in $Cu_{1-x}Zn_xFe_2O_4$ Nano-Interlayers for High-Performance Cu/p-Si MIS Schottky Ultraviolet Photodiodes

K U Aiswarya
Sree Keralavarma College,
Arun K J
drarunkj@gmail.com

Sree Keralavarma College,
M D Aggarwal
Alabama Agricultural and Mechanical University
Padmaja Guggilla
Alabama Agricultural and Mechanical University

Research Article

Keywords: Schottky barrier diodes, Ferrite thin films, MIS diodes, Interfacial layer

Posted Date: September 14th, 2026

DOI: https://doi.org/10.21203/rs.3.rs-10806867/v1

License: This work is licensed under a Creative Commons Attribution 4.0 International License.
Read Full License

Additional Declarations: No competing interests reported.

Composition-Driven Defect and Interface Engineering in $Cu_{1-x}Zn_xFe_2O_4$ Nano-Interlayers for High-Performance Cu/p-Si MIS Schottky Ultraviolet Photodiodes

Aiswarya K U[1], K J Arun[1]*, M D Aggarwal[2], Padmaja Guggilla[2]

[1]Department of Physics, Sree Kerala Varma College, Thrissur, 680011, University of Calicut, Kerala, India.

[2]Department of Physics, Alabama A & M University, Normal, Alabama 35811, USA.

email: drarunkj@gmail.com

Abstract

Engineering defect chemistry and interface quality in nano-interlayers is an effective strategy for improving carrier transport in metal–insulator–semiconductor (MIS) photodiodes; however, the influence of composition-controlled defect engineering in ferrite nano-interlayers remains insufficiently explored. In this work, $Cu_{1-x}Zn_xFe_2O_4$ (x = 0.2–0.8) nano-interlayers were synthesized by chemical bath deposition and employed as interfacial insulating layers in Cu/p-Si MIS Schottky photodiodes. Zn substitution was utilized as a composition-driven defect and interface engineering approach to systematically tailor the structural, optical and electronic properties of the ferrite layer. Structural and morphological analyses reveal progressive crystallinity enhancement, grain growth and reduced lattice strain with increasing Zn concentration, while optical studies demonstrate band-gap narrowing from 3.68 to 3.50 eV, promoting enhanced ultraviolet light absorption. X-ray photoelectron spectroscopy confirms oxygen-vacancy-related defect states and mixed valence species that facilitate charge transfer and improve interface quality. These interconnected structural and electronic modifications reduce carrier trapping and recombination, leading to lower ideality factors and enhanced barrier homogeneity. Consequently, the optimized Cu/ $Cu_{0.2}Zn_{0.8}Fe_2O_4$ /p-Si photodiode exhibits a responsivity of 65.9 mA W^{-1}, quantum efficiency of 25.5% and detectivity of 2.41 × 10^{11} Jones under ultraviolet illumination. The present work establishes a comprehensive structure–defect–interface–performance relationship, demonstrating that composition-controlled defect engineering offers a practical design strategy for high-performance ferrite-based silicon photodiodes and other optoelectronic devices.

Keywords: Schottky barrier diodes, Ferrite thin films, MIS diodes, Interfacial layer

1. Introduction

In the recent years researchers have developed a keen interest in the experimental studies of metal-semiconductor (MS) and metal-insulator-semiconductor (MIS) Schottky barrier diodes (SBDs) due to their vast applications in modern device technology [1]. The formation of interfacial layer between metal and semiconductor is important as it serves as a dielectric medium which prevent the inter-diffusion between MS junctions and levitate the issues of electric field reduction in MS diodes thereby influencing the electrical parameters, performance, stability and reliability of the

device [2]. The appropriate choice of interfacial insulating layer and its deposition conditions are important as the performance of the diodes depends on interface quality, surface preparation, formation of barrier height at MS interface, sample temperature, thickness and permittivity of interfacial layer [3]. From the literature it is evident that the barrier height could be either increased or decreased by using an interfacial layer in the M-S interface [4]. Due to the simple fabrication and multipurpose usage of MIS structured SBDs, they are the potential components in solar cells, photodetectors, Zener diodes, microwave mixers, varactors, sensors, radio frequency attenuators, rectifiers, capacitors, photo voltaic energy converters, photodiodes, phototransistors and several integrated circuits [5-7].

Ferrites in nanosized form can be used as the interfacial layer owing to their excellent electrical, optical and magnetic properties [8]. The general formula to represent ferrites is MFe_2O_4 where M represents divalent cation such as Cu, Zn, Ni, Mg, Mn, Co etc [9]. Ferrites have incredible applications in electromagnetic wave absorption, ferromagnetic fluids, high-density information storage devices, targeted drug delivery systems, high- frequency electronic devices, magnetic separation, MRI, gas sensors, magnetic refrigeration systems etc [10-15]. Ferrites in the thin film form can be synthesized by employing the deposition techniques such as spin coating, dip coating, pulsed laser deposition, RF sputtering, spray pyrolysis, chemical bath deposition, sol-gel method etc [16-18]. The magnetic, optical and electric properties of the ferrites are strongly dependent on their chemical compositions, temperature and substitutions [19]. Thin films of ferrites belonging to the series $Cu_{1-x}Zn_xFe_2O_4$ (x= 0.2, 0.4, 0.6, 0.8) are synthesized using chemical bath deposition due to its simplicity, reduced cost and lesser number of precursors. $Cu_{1-x}Zn_xFe_2O_4$ are used in magnetic recording media, antennas, microwave latching devices, sensor, switches, radio frequency coil, transformer cores, circulators, gyrators, high-density information storage devices and phase shifters etc. due to the high electrical resistivity, low eddy current loss, low dielectric loss and excellent soft magnetic properties [20-25]. These mixed ternary oxides (or binary ferrites) show more diverse properties than the original unsubstituted ferrite [26]. The Cu^{2+} ions occupy the octahedral sites and Zn^{2+} ions occupy the tetrahedral sites while Fe^{3+} ions can occupy both tetrahedral and octahedral sites [27,28].

In the present work, composition-driven $Cu_{1-x}Zn_xFe_2O_4$ nano-interlayers were synthesized through a simple chemical bath deposition method and employed as interfacial insulating layers in Cu/p-Si MIS Schottky photodiodes. Instead of considering Zn substitution merely as compositional modification, this work demonstrates its role as an effective defect and interface engineering strategy. By systematically correlating structural evolution, morphology, optical band-gap modulation, oxygen vacancy formation, electrical transport characteristics and photodiode performance under different illumination intensities and operating temperatures, a comprehensive structure–defect–interface–performance relationship is established. The study demonstrates that controlled interface engineering through Zn substitution provides a simple and scalable approach for enhancing carrier transport, suppressing recombination losses and improving ultraviolet photodetection performance in ferrite-based silicon optoelectronic devices.

Despite the extensive investigations on ferrite nanomaterials and metal–insulator–semiconductor (MIS) Schottky diodes, most previous studies have primarily focused on improving device performance through the selection of different interfacial dielectric materials or by optimizing fabrication conditions. Comparatively little attention has been devoted to understanding how composition-driven defect engineering within ferrite nano-interlayers influences the

structural evolution, interface quality, charge transport and ultimately the photodetection performance of MIS devices. In particular, the influence of Zn substitution on oxygen vacancy formation, lattice distortion and barrier homogeneity, and the resulting structure–defect–interface–performance relationship in Cu/ $Cu_{1-x}Zn_xFe_2O_4$/ p-Si MIS photodiodes has not been systematically established. Addressing this knowledge gap is essential for the rational design of high-performance silicon-compatible photodetectors.

2. Experimental

2.1 Preparation of $Cu_{1-x}Zn_xFe_2O_4$ thin films

An aqueous solution of Zinc chloride, Copper chloride and Ferric chloride with adequate stoichiometry were prepared, mixed together and stirred continuously at 80˚C for 1 hour to get homogeneous solution. Then aqueous ammonia was added dropwise to adjust the pH of the solution. $Cu_{1-x}Zn_xFe_2O_4$ with varying x concentration were prepared (x= 0.2, 0.4, 0.6, 0.8) and immersed the cleaned substrate vertically in the prepared chemical bath as shown in Fig. 1. The entire system was kept in a water bath at 70˚C for 10 hours. The coated films were dried and later annealed at 500˚C for 3 hours. Brown colored thin films obtained were $Cu_{0.8}Zn_{0.2}Fe_2O_4$, $Cu_{0.6}Zn_{0.4}Fe_2O_4$, $Cu_{0.4}Zn_{0.6}Fe_2O_4$, $Cu_{0.2}Zn_{0.8}Fe_2O_4$ and named as CZF1, CZF2, CZF3 and CZF4 respectively.

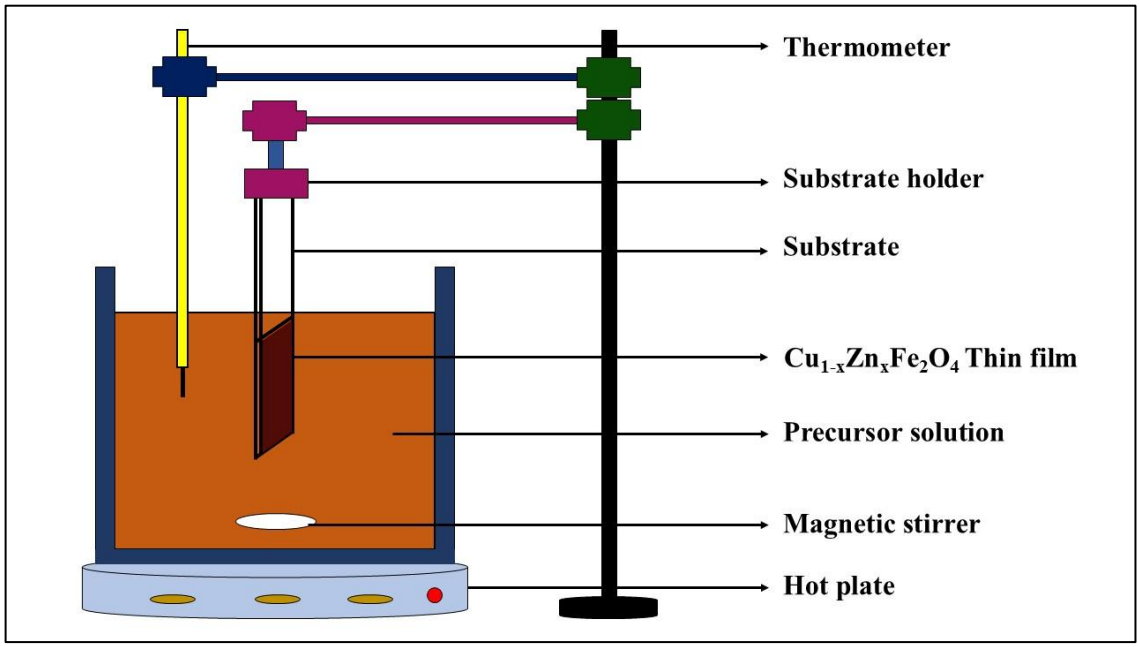


Fig. 1 Schematic diagram of preparation of thin interfacial film layer by Chemical bath deposition method

2.2 Fabrication of Cu/ $Cu_{1-x}Zn_xFe_2O_4$ / p-Si SBDs

The $Cu_{1-x}Zn_xFe_2O_4$ were deposited on well cleaned p-Si wafers (100) by chemical bath deposition. The fabricated films were annealed at 60˚C for 2 hours. DC magnetron sputtering (HIND high vacuum-BC 300) was used to deposit Copper (Cu) metal on the $Cu_{1-x}Zn_xFe_2O_4$ / p-Si films by to fabricate Cu/ $Cu_{1-x}Zn_xFe_2O_4$ / p-Si SBDs as shown in Fig. 2.

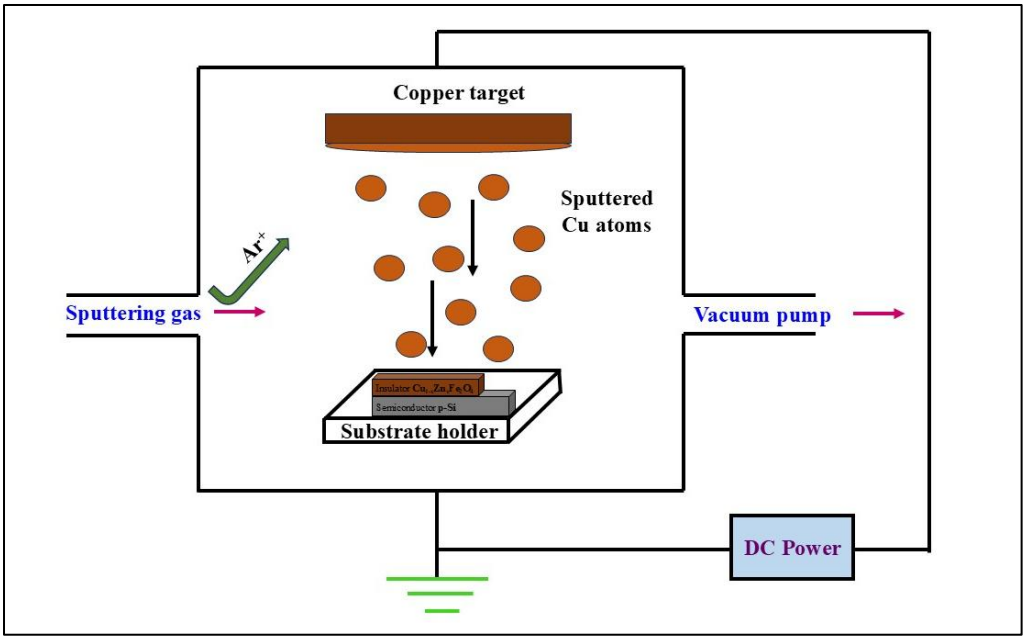


Fig. 2 Schematic diagram of Sputtering set up for the coating of metal electrode layer

3. Results and Discussion

3.1 X-ray Diffraction (XRD) analysis

X-ray diffraction spectra of $Cu_{1-x}Zn_xFe_2O_4$ thin films recorded by Bruker D8 advanced XRD machine by using CuKα radiation (1.541Å) over a 2θ range of 10º to 80º is shown in Fig. 3. All the diffraction peaks from the XRD pattern can be indexed with the single-phase cubic spinel structure of $CuFe_2O_4$ (ICDD cardno:72–1174) and $ZnFe_2O_4$ (ICDD card no: 89–1012) [29]. All four samples exhibit peaks at similar 2θ positions, suggesting that the same crystalline phases are present across the samples. The peaks are relatively broad, suggesting that the crystallite size in the samples is small. Small shifts in peak positions indicate changes in the crystalline behaviour [30]. Such peak shifts are characteristic of successful compositional tuning in spinel ferrites and indicate local lattice distortion accompanied by changes in cation distribution. Absence of the diffraction peaks of other species confirms the purity of the synthesized samples [31].

The average crystallite size of the thin films is evaluated using Scherrer equation [32]

$$D = \frac{K\lambda}{\beta\cos\theta} \quad (1)$$

where D, θ, K, λ and β are the mean crystallite size (nm), Bragg's angle, crystallite shape factor (0.9), wavelength of X-ray (1.541 Å) and full width at half maximum (FWHM). The average crystallite size obtained from the Scherrer method for CZ1, CZF2, CZF3 and CZF4 are 6.21 nm, 13.74 nm, 30.17 nm and 42.79 nm. This is due to the variation of ionic size of the $Zn^{2+}$and Cu^{2+} cations as the ionic size of Zn^{2+} (0.80 Å) is larger than that of Cu^{2+} (0.70 Å) [33]. Large crystallite size indicates higher crystallinity, suggesting a more ordered atomic arrangement.

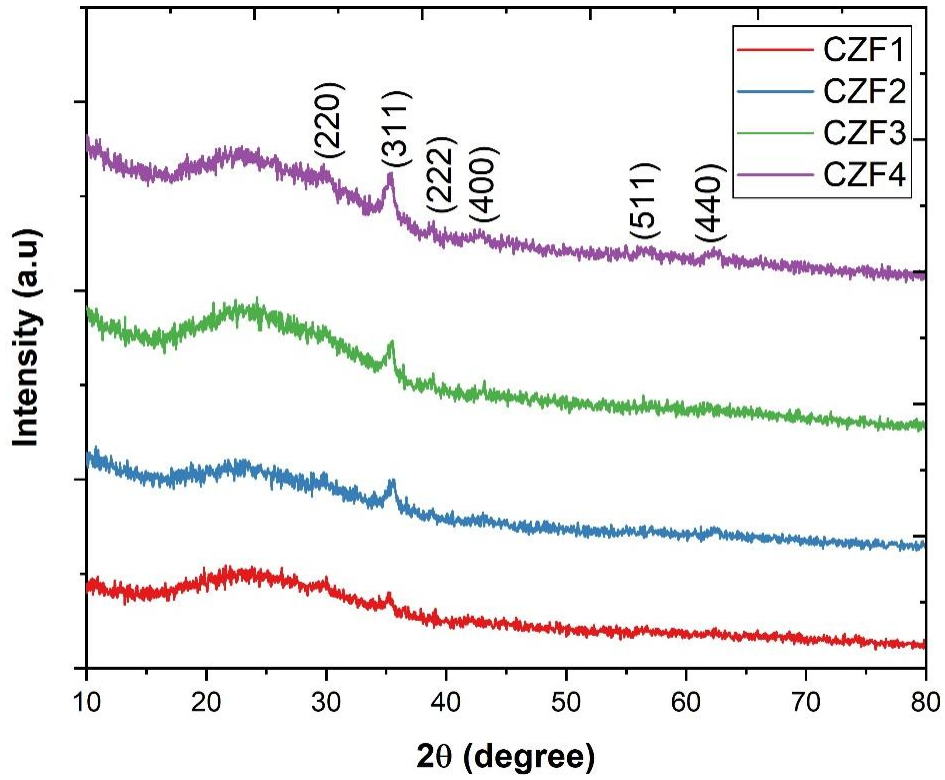


Fig. 3 X-ray diffraction pattern of $Cu_{1-x}Zn_xFe_2O_4$ thin films

The micro-strain (ε), dislocation density (δ) and stacking fault (SF) of the $Cu_{1-x}Zn_xFe_2O_4$ thin films are evaluated using the following equations (2)– (4).

$$\varepsilon = \beta \frac{cos\theta}{4} \quad (2)$$

$$\delta = \frac{1}{D^2} \quad (3)$$

$$SF = \left[\frac{2\pi^2}{45(3tan\theta)^{\frac{1}{2}}}\right]\beta \quad (4)$$

The Table.1 shows the structural parameters evaluated for the $Cu_{1-x}Zn_xFe_2O_4$ thin films. The strain and dislocation density in the films decreases as the concentration of Zn^{2+} increases because the defects in the lattice are removed. CZF4 films with good crystallinity and less strain are interesting because they have active centers that can improve the diode's photo responsivity.

Sample	Crystallite size D (nm)	Dislocation density (δ) x 10^{15} (lines/m^2)	Micro strain (ε)	Stacking fault (SF)
CZF1	6.21	14.274	0.0058	0.0103
CZF2	13.74	5.289	0.0029	0.0052
CZF3	30.17	1.098	0.0024	0.0053
CZF4	42.79	0.546	0.0008	0.0016

Table. 1 The structural parameters of $Cu_{1-x}Zn_xFe_2O_4$ thin films

The progressive increase in crystallite size accompanied by the simultaneous reduction in lattice strain and dislocation density indicates that Zn substitution effectively improves the structural ordering of the ferrite lattice. Such structural evolution is expected to decrease grain-boundary scattering and reduce the density of crystallographic defects acting as carrier trapping centers. Consequently, charge carriers can traverse the nano-interlayer more efficiently, improving charge transport across the MIS interface. Furthermore, the reduced structural disorder contributes to a more homogeneous Schottky barrier and suppresses interface recombination, thereby providing the structural basis for the enhanced electrical and photodetection characteristics observed in the optimized Cu/CZF4/p-Si device. The simultaneous increase of the crystallite size and the decrease of the lattice imperfections are important for the performance of devices. Improved crystallinity reduces scattering at grain boundaries and reduces structural defects and act as carrier trapping centers. This facilitates charge carriers to diffuse more efficiently through the $Cu_{1-x}Zn_xFe_2O_4$ nano interlayer, thus improving the charge transport at the MIS interface. The lower defect density is also expected to reduce the recombination at the interface, thus contributing to the lower ideality factor, higher barrier homogeneity and improved photoresponse for the MIS photodiode. This structural evolution agrees with the recent reports on composition engineered ferrite nanomaterials, where controlled cation substitution may enhance the crystallinity, reduce the lattice strain and improve the electrical and optoelectronic performance of ferrite-based devices. Thus, the present results show that Zn substitution is not only a compositional modifier but also an effective tool for defect and interface engineering and provides the structural basis for the improved photodiode properties.

3.2 Field-Emission Scanning Electron Microscopy- Energy Dispersive X-ray spectroscopy (FESEM- EDX) analysis

The FESEM images of $Cu_{1-x}Zn_xFe_2O_4$ thin films are shown in Fig. 4. FESEM images consist of the grains appearing as irregular plate or flake-like and quasi-spherical crystallites, forming clustered assemblies in the nanometer regime. No large cracks or voids are observed, indicating good film continuity. Fig. 4a represents fine nanograins attached to larger clusters, suggesting incomplete grain growth. This morphology is usually associated with the presence of lower Zn concentration where nucleation dominates over grain growth. Lower Zn concentration enhances the nucleation rate resulting in smaller crystallites and porous texture. In Fig. 4b, the particles appear slightly more compact compared to Fig. 4a. The grain boundaries are more distinguishable and the distribution is relatively improved. As the Zn content increases, diffusion and grain coalescence enhances leading to improved packing. Fig. 4c shows well-defined plate/flake-like crystallites with better uniformity. The particle size appears slightly increased and the surface is denser. The film shows reduced porosity compared to Fig. 4a and Fig. 4b. With increasing Zn concentration, crystallinity and grain growth enhances resulting in better structural ordering. The Fig. 4c corresponds to minimum lattice strain and improved spinel stabilization. Fig. 4d displays densely packed plate-like structures. Higher Zn concentration leads to strong particle coalescence with increased grain size and enhanced grain growth. Such morphology is expected to improve interfacial contact between the Cu electrode and the ferrite nano interlayer while simultaneously reducing localized electric-field fluctuations caused by surface irregularities. Consequently, the CZF4-based MIS photodiode demonstrates superior electrical characteristics. This trend is consistent with dopant-induced lattice distortion and enhanced diffusion kinetics during film formation. FESEM observed grain growth with increasing Zn content strongly

agrees with XRD results. The gradual evolution from loosely packed nanograins to dense and well-connected plate-like crystallites demonstrates that Zn substitution promotes grain coalescence and improves film continuity. A compact nano-interlayer minimizes structural discontinuities at the metal–insulator interface and provides continuous pathways for carrier transport. The improved interface uniformity also suppresses localized electric-field fluctuations and reduces carrier trapping at grain boundaries. Such morphological optimization contributes directly to the lower ideality factor, higher barrier homogeneity and enhanced photocurrent observed in the fabricated MIS photodiodes.

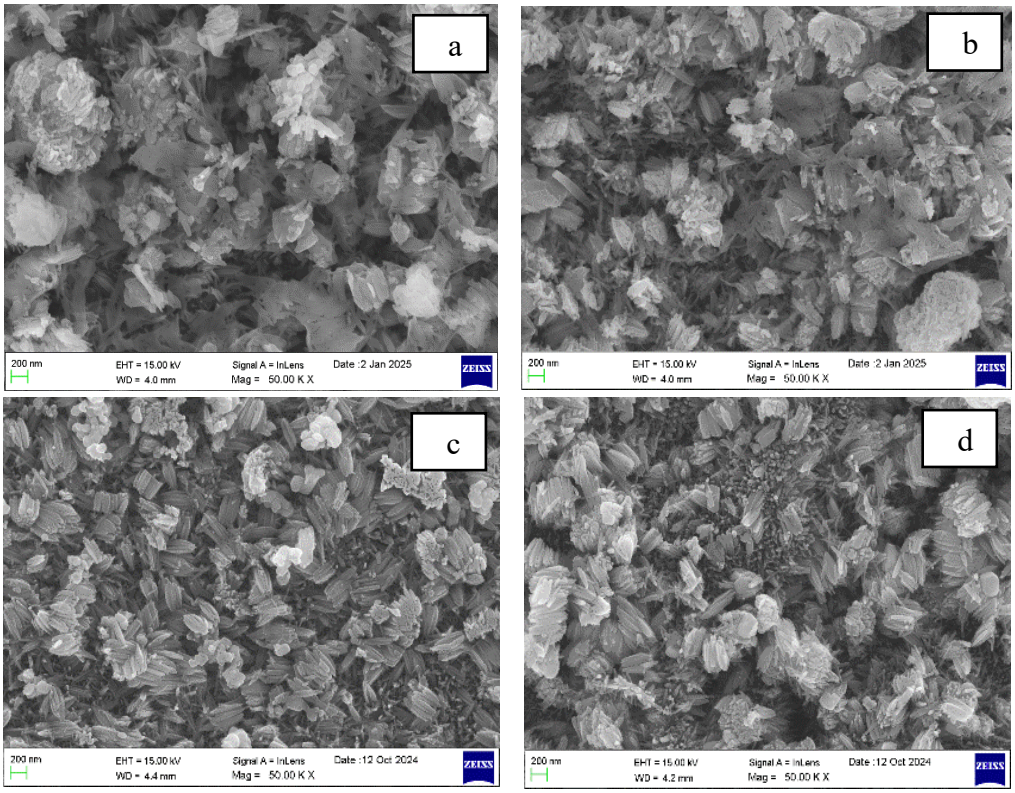


Fig. 4 FESEM images of (a) CZF1 (b) CZF2 (c) CZF3 (d) CZF4

Fig. 5 shows the EDX spectra of $Cu_{1-x}Zn_xFe_2O_4$ thin films. It confirms that all the films consist of Cu, Zn, Fe and O only. Absence of any other element confirms the purity of the samples and the reliability of the synthesis route adopted [34]. The cross-sectional FESEM of the Cu/ $Cu_{1-x}Zn_xFe_2O_4$ /p-Si diode is given in the Fig. 6. The thickness of the $Cu_{1-x}Zn_xFe_2O_4$ film is 440nm and the Cu layer is 210 nm. Quantum mechanical tunneling of the electrons occurs through potential barriers at small thicknesses. At greater thicknesses, SCLC (space-charge-limited current) takes over as a space charge region is created due to the accumulation of the injected carriers inside the material. The current drops as the oxide thickness rises above a critical thickness.

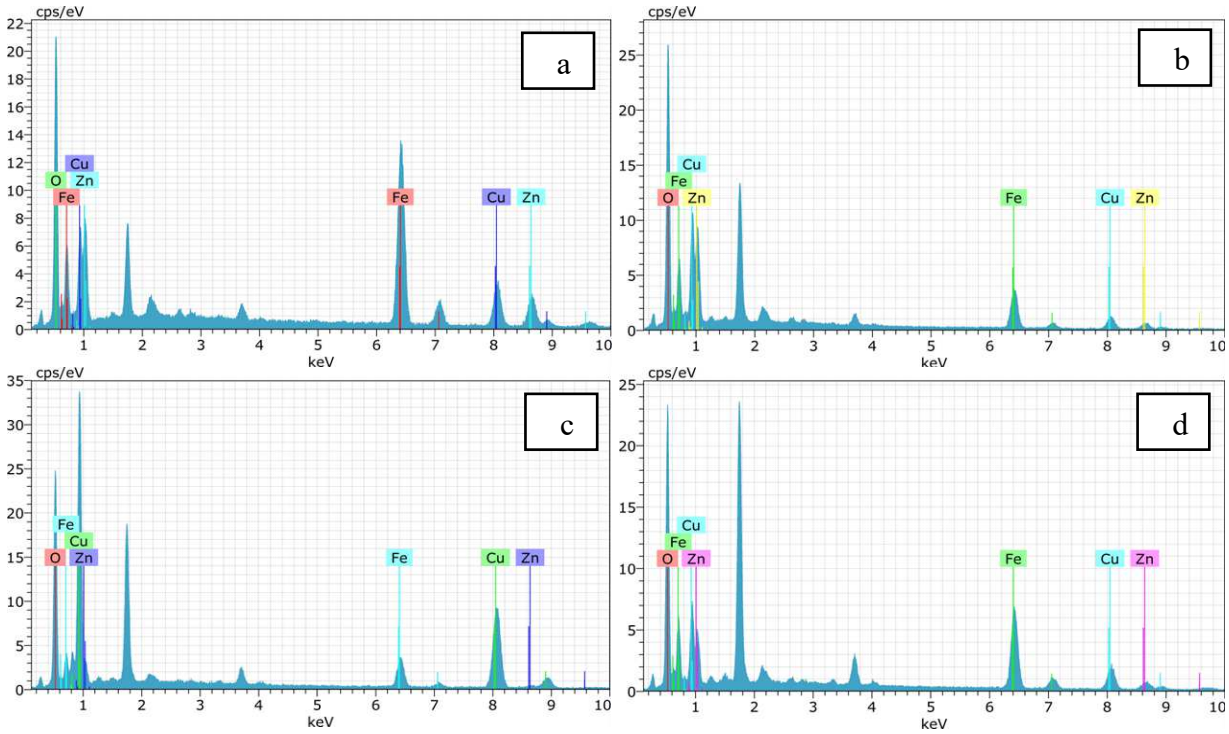


Fig. 5 EDX spectra of (a) CZF1 (b) CZF2 (c) CZF3 (d) CZF4

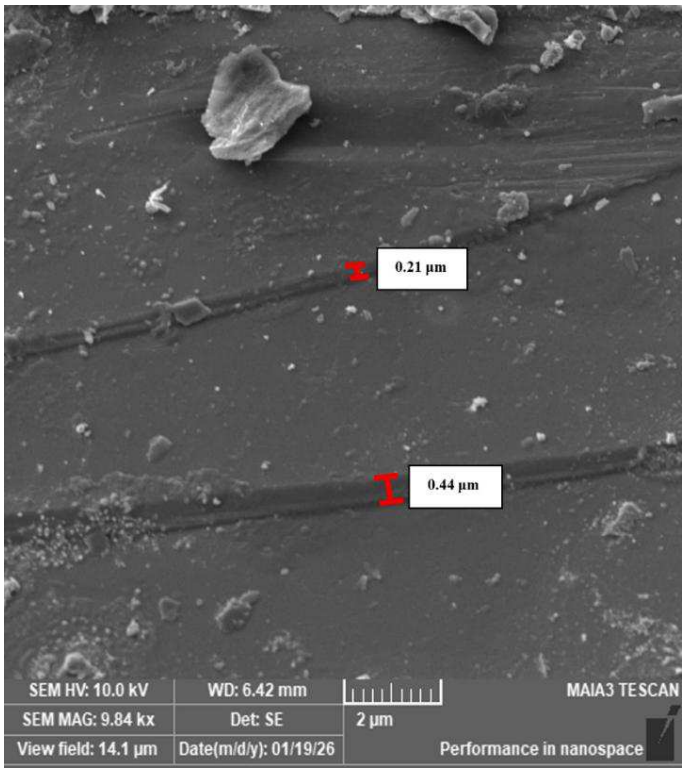


Fig. 6 Cross sectional FESEM images of fabricated Cu/ $Cu_{1-x}Zn_xFe_2O_4$ /p-Si diode

3.3 The UV-VIS-NIR absorption spectroscopy

The absorbance spectra of all the films recorded between 200 nm and 1500 nm are shown in Fig. 7. All four samples exhibit a significant absorption peak in the UV region around 200- 300 nm. As wavelength increases beyond 300 nm, the absorbance decreases and then stabilizes towards the higher wavelength [35]. Absorbance remains non-zero in the visible and NIR regions indicating that the samples still absorb some light in these regions, although to a lesser extent than in the UV. The absorption intensity is found to be increasing significantly with an increase in Zn concentration. This is indicative of the enhanced interaction between the incident photons and the ferrite nano interlayers. Such behaviour is attributed to the better crystallinity, larger crystallite size and the modification of the electronic structure due to the Zn substitution. The energy band gap of the samples is found using the Tauc relation [36]

$$(\alpha h\nu)^n = A(h\nu - E_g) \quad (5)$$

where E_g, A, α, h, ν and n are band gap energy, constant that depends on the transition probability, coefficient of absorbance, Planck's constant, frequency and constant that depends on the band gap type. The energy gap of CZF1, CZF2, CZF3 and CZF4 found using Tauc plot from Fig. 8 are 3.68 eV, 3.63 eV, 3.60 eV and 3.50 eV respectively. The reduction in band gap can be attributed to the change in the crystalline potential, band tailing or broadening of impurity band to merge at the bottom of the conduction band upon increasing the zinc content in the samples [37]. A narrower band gap enhances the probability of photon absorption under ultraviolet illumination, leading to increased photogenerated electron–hole pairs and higher photocurrent generation. Talaat M. Hammad et.al [38] synthesized $Cu_{1-x}Zn_xFe_2O_4$ (x = 0.0, 0.2, 0.4, 0.6, 0.8 and 1) ferrites and reported that the direct energy band gap values of the samples are in between 3.64 to 3.10 eV with increase in the concentration of Zn^{2+}. The decrease in the band gap by increasing the Zn content was reported by Chen et al [39], Wang et al [40] and Yogo et al [41].

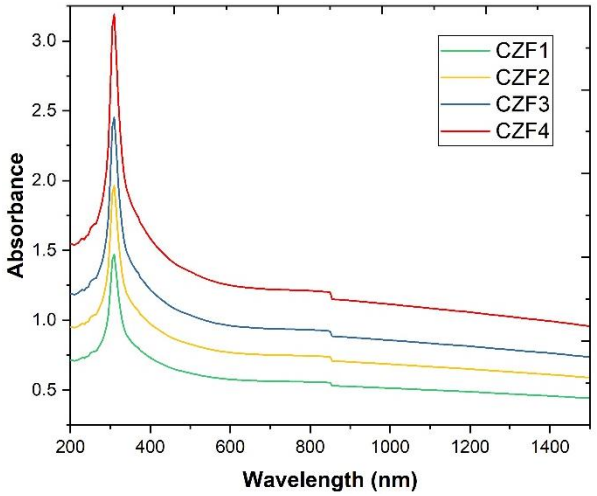


Fig. 7 UV-VIS-NIR absorbance spectra

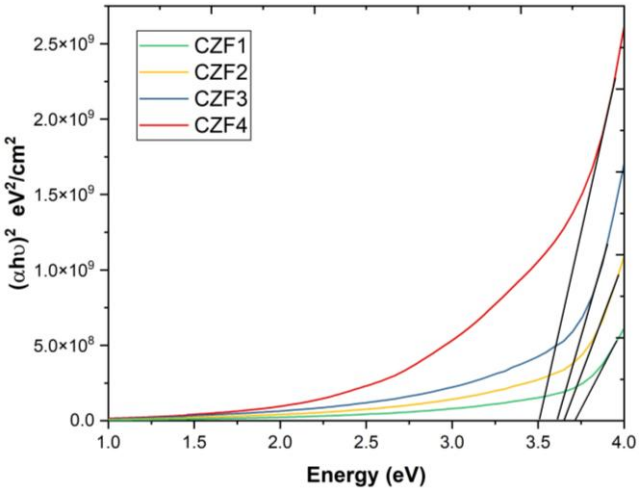


Fig. 8 Plot of optical band gap energy

Absorption coefficient (α), extinction coefficient (k) and optical conductivity (σ_{opt}) of $Cu_{1-x}Zn_xFe_2O_4$ thin films evaluated using the following equations (6- 8) are listed in Table. 2.

$$\alpha = \frac{ln\left(\frac{1}{T}\right)}{t} \quad (6)$$

$$k = \frac{\alpha\lambda}{4\pi} \quad (7)$$

$$\sigma_{opt} = \frac{nc\alpha}{4\pi} \quad (8)$$

where t, n, c, λ and T are the thickness of the film, refractive index, velocity of the light, wavelength of light and transmittance. The α and k increases with Zn^{2+} concentration. The production of electron-hole pairs increases as α rises, because more photons are trapped in the films. An essential metric for analyzing the allowed interband optical transitions is the optical conductivity. For CZF4, the highest value of σ_{opt} =7.366 x 10^{14} S/cm is obtained, indicating the strong photo response of the material. The gradual narrowing of the optical band gap with increasing Zn concentration reflects modification of the electronic structure through cation redistribution and defect-induced band-tail states. The reduced band gap facilitates more efficient ultraviolet photon absorption, resulting in enhanced generation of electron–hole pairs within the ferrite nano-interlayer. Simultaneously, the increased absorption coefficient and optical conductivity indicate improved interaction between the incident photons and the semiconductor, thereby facilitating efficient carrier generation and transport. These optical modifications directly contribute to the enhanced responsivity and quantum efficiency observed for the CZF4-based photodiode.

Sample	Absorption coefficient (α) x 10^7 (cm^{-1})	Extinction coefficient (k)	Optical bandgap (E_g) (eV)	Optical conductivity (σ_{opt}) x 10^{14} (S/cm)
CZF1	1.13	0.27	3.68	2.74
CZF2	1.50	0.37	3.63	3.89
CZF3	1.88	0.46	3.60	5.18
CZF4	2.44	0.60	3.50	7.36

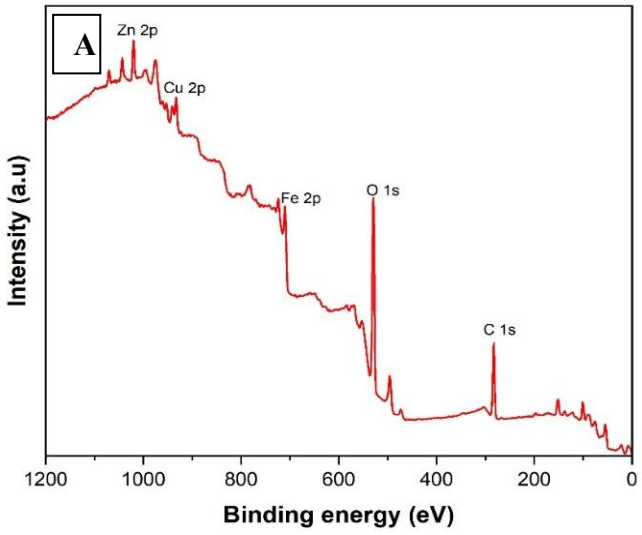
Table. 2 The optical parameters of $Cu_{1-x}Zn_xFe_2O_4$ thin films

3.4 XPS Analysis

XPS analysis is used for the investigation of surface composition, electronic structures and chemical states of the samples. The C 1s at 284.8 eV is used as the calibration peak and is due to the presence of adventitious carbon deposition on the samples. The XPS survey spectrum indicates that the sample contains the elements Zinc (Zn), Copper (Cu), Iron (Fe) and Oxygen (O) as expected and is represented in Fig. 9. The presence of Fe $2p_{3/2}$ peak at 710.5 eV, shake-up satellite structure at 718.6 eV and Fe $2p_{1/2}$ peak at 724.5 eV is confirmed from the Fe 2p XPS spectra [42]. Difference in the binding energy between the doublets confirms the element and the binding energy value confirms the chemical state [43]. S. Wang et.al [44] observed the shake up satellite peak of Fe appears at 718 eV which confirms the presence of maghemite or hematite (Fe^{3+}). The deconvoluted spectrum of Fe $2p_{3/2}$ shows three peaks having binding energies at 710.08, 711.15 and 712.78eV which can be attributed to octahedral Fe (II), octahedral Fe (III) and tetrahedral Fe (III) respectively [45]. From the XPS spectrum of the Cu 2p, the presence of two main peaks along with satellite features are observed. The presence of Cu $2p_{3/2}$ at 932.5 eV and Cu $2p_{1/2}$ peak at 953.2 eV is confirmed. The deconvoluted spectrum of Cu $2p_{3/2}$ shows two peaks having binding energies at 932.55 and 934.1eV which can be attributed to Cu (I) and Cu (II) respectively [46]. The existence of satellite peaks at higher binding energy side of the main Cu 2p peaks is an indication of the presence of Cu^{2+} ions. These satellite peaks arise from charge transfer transitions in compounds with Cu^{2+} ions. The XPS spectrum of Zn 2p shows two strong peaks at 1044.9 eV and 1021.9eV that can be attributed to Zn $2p_{1/2}$ and Zn $2p_{3/2}$, which suggest that zinc is present in the Zn^{2+} oxidation state

[44]. The peaks are relatively sharp, indicating a single chemical state of zinc. The XPS spectrum of O 1s provides information about the oxygen-containing species and their chemical environments within the sample. Oxygen can exist in various forms and each has a slightly different binding energy. The three characteristic peaks located at 530.05 eV, 531.04 eV and 532.48 eV are assigned as the lattice oxygen, non- lattice oxygen and absorbed oxygen respectively [47]. The peak of 531.04 eV is closely related to surface oxygen vacancies such as non-lattice oxygen, rather than the lattice oxygen and they play a major role in stabilizing the lattice disorder by passivating the dangling bonds [48]. The localized defect states produced by oxygen vacancies change the binding energies of neighboring oxygen atoms, causing a noticeable shift in the position and intensity of the O 1s peak. The surface oxygen vacancies play a crucial role in improving light absorption, charge separation and the availability of reactive sites for chemisorption [49]. The existence of oxygen vacancies can also contribute to increase the hydrophilicity. The oxygen vacancies revealed by XPS not only change the local electronic structure of $Cu_{1-x}Zn_xFe_2O_4$, but also the electrical behavior of the MIS junction. These vacancies act as shallow donor-like defects to increase the carrier concentration and enhance the interfacial charge transfer. This leads to reduced carrier trapping, lower recombination probability and enhanced photocurrent generation. This interpretation is in line with recent reports highlighting defect engineering as a powerful way to improve the performance of semiconductor photodetectors.

Thus, XPS analysis provides direct evidence that Zn substitution not only modifies the chemical composition but also alters the defect chemistry of the ferrite nano-interlayer. In particular, the oxygen-vacancy-related component of the O 1s spectrum indicates the formation of localized donor-like defect states near the conduction band. These oxygen vacancies facilitate charge transfer by increasing carrier concentration and providing intermediate energy levels for trap-assisted transport across the ferrite/Si interface. Simultaneously, the improved crystallinity minimizes deep defect states responsible for carrier recombination. The combined effect of optimized oxygen vacancy concentration and reduced structural disorder promotes efficient separation and extraction of photogenerated charge carriers, thereby resulting in lower ideality factors, higher barrier homogeneity and significantly improved photodetection characteristics. These findings clearly demonstrate that defect engineering through controlled Zn substitution governs the electronic behaviour of the $Cu/Cu_{1-x}Zn_xFe_2O_4/p$-Si MIS junction.



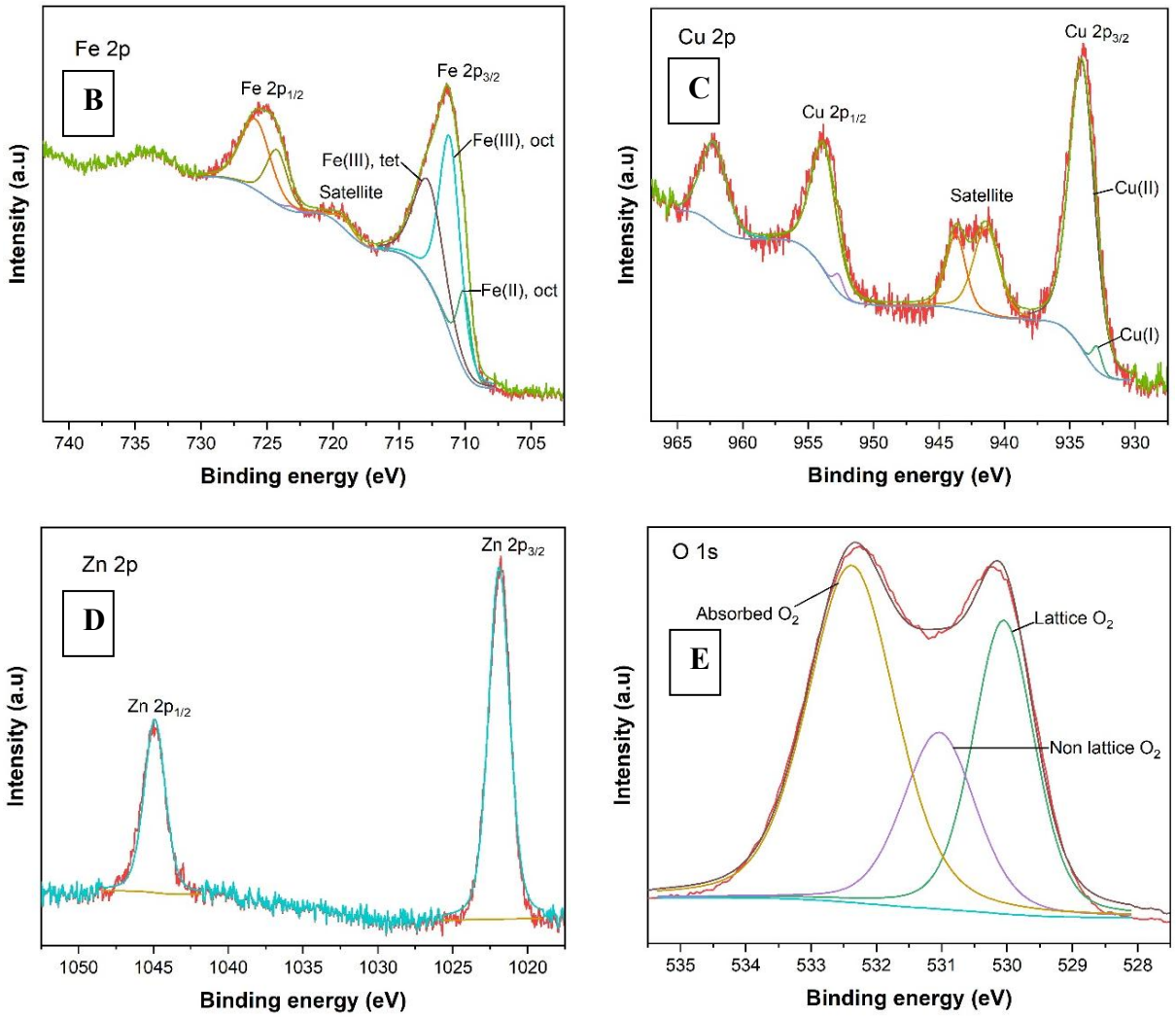


Fig. 9 The XPS spectra of $Cu_{1-x}Zn_xFe_2O_4$: (A) survey scan, (B) Fe2p (C) Cu 2p (D) Zn 2p and (E) O 1s

3.5 DC electrical analysis

The dc electrical conductivity of the $Cu_{1-x}Zn_xFe_2O_4$ thin films is calculated by measuring the I-V characteristics using two probe Keithley source meter 2450 by varying temperature as given in Fig. 10. It can be seen that current increases linearly with voltage from 5 V to 40 V for all the samples [50]. The current increases with the temperature in all films as mobility of electrons increases when it absorbs the heat energy [51].

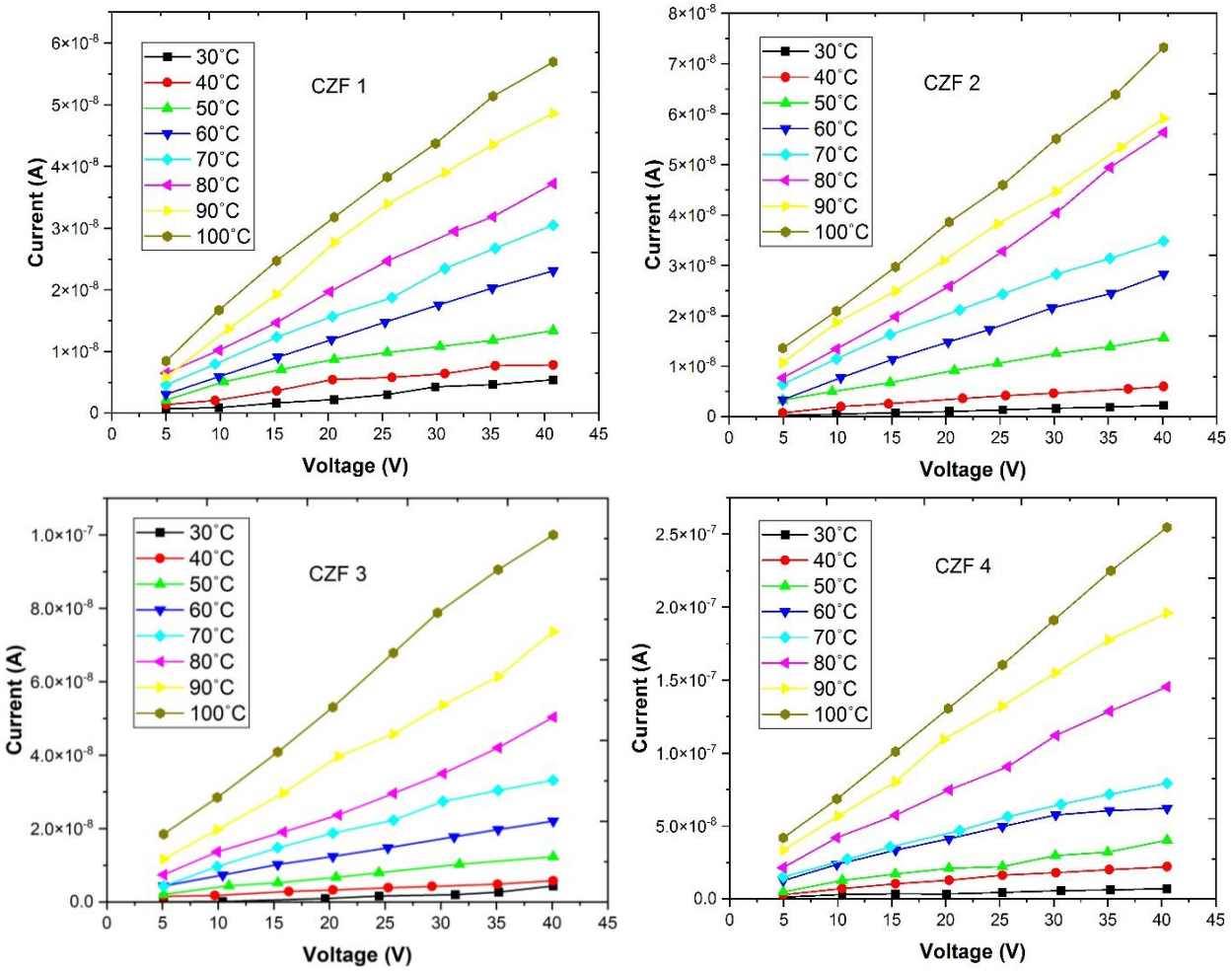


Fig. 10 I–V characteristics of the $Cu_{1-x}Zn_xFe_2O_4$ thin films

The conductivity (σ) is calculated using the following equation [4]

$$\sigma_{dc} = \frac{t}{RA} \tag{9}$$

where A, t and R are area, thickness and resistance of the films. As zinc concentration rises, the average resistivity of the films reduces. The decrement in average resistivity is usually due to increased grain size, improved crystallinity, reduced defects and impurities when zinc content is increased. The lower resistivity can improve the rectification in the fabricated SBDs [52]. The average conductivity increases with zinc concentration. Conductivity values vary from 1.24×10^{-14} S/cm to 5.53×10^{-14} S/cm indicating the insulating behaviour of the films thereby making it an appropriate material for interfacial layer [53].

The activation energy of the films can be calculated from the slope of the Arrhenius plot as given in Fig. 11 using the equation [54]

$$\sigma = \sigma_0 \exp\left(\frac{-E_a}{k_B T}\right) \tag{10}$$

where E_a, k_B and σ_0 are activation energy, Boltzmann constant and pre-exponential factor. The evaluated values of conductivity, resistivity and activation energy are listed in Table. 3. The average activation energy values reduces with increasing Zn^{2+} concentration.

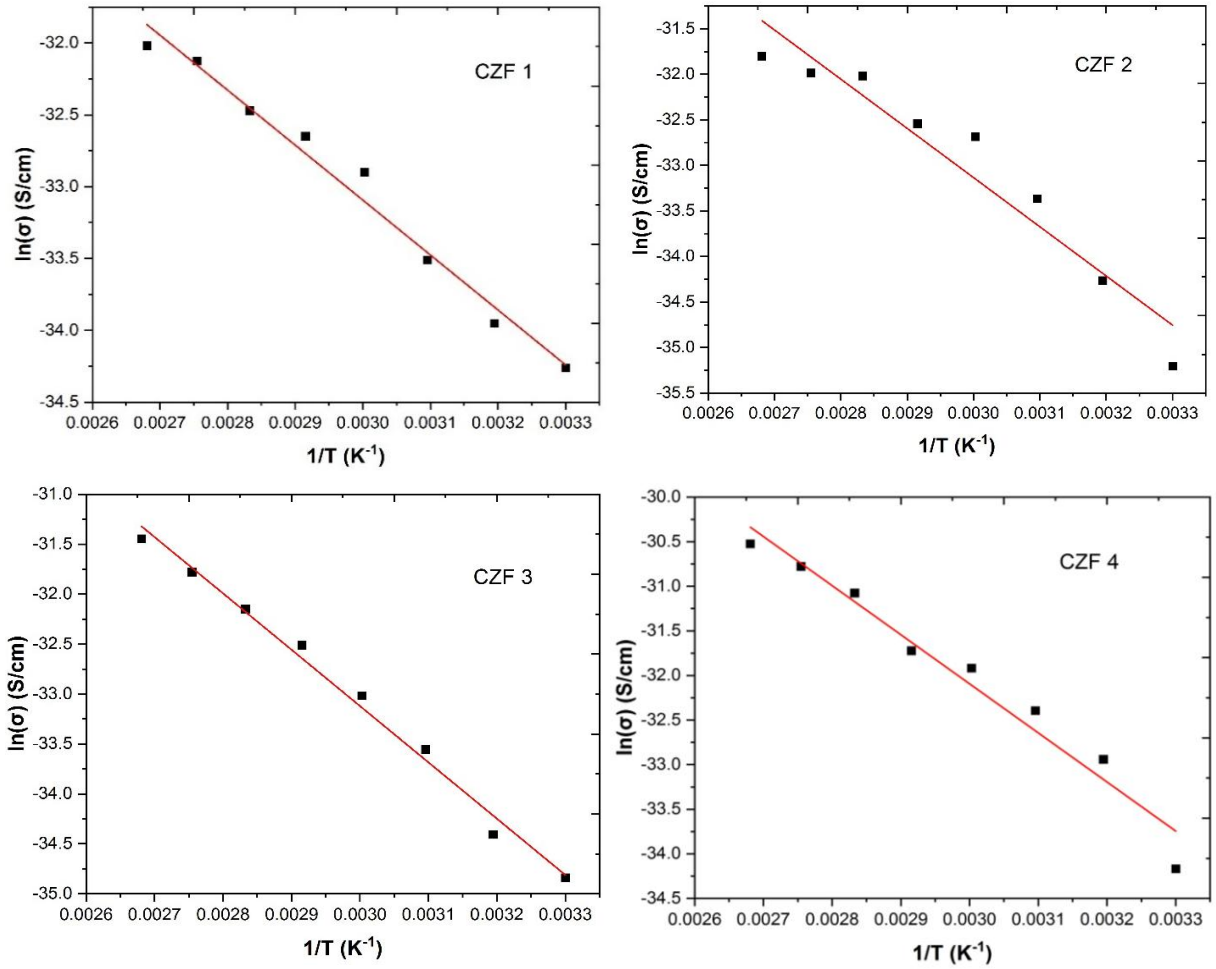


Fig. 11 Arrhenius plots of 1/T vs. ln (σ) for $Cu_{1-x}Zn_xFe_2O_4$ thin films

Sample	Resistivity (ρ) (Ωcm)	Conductivity (σ_{dc}) (S/cm)	Activation energy (E_a) (eV)
CZF1	8.95×10^{13}	1.24×10^{-14}	0.561
CZF2	6.47×10^{13}	1.54×10^{-14}	0.518
CZF3	4.53×10^{13}	2.20×10^{-14}	0.391
CZF4	3.13×10^{13}	5.53×10^{-14}	0.322

Table. 3 The electrical parameters of $Cu_{1-x}Zn_xFe_2O_4$ thin films

The improvement in electrical conductivity with increasing Zn concentration originates from the combined influence of enhanced crystallinity, reduced lattice disorder and defect-assisted carrier transport. Although the ferrite films preserve their insulating nature, which is essential for efficient MIS operation, the moderate increase in conductivity facilitates carrier transport across the nano-interlayer without compromising the Schottky barrier. Therefore, the optimized electrical characteristics arise from a balanced combination of sufficient insulation for barrier formation and adequate carrier transport through the defect-engineered ferrite layer.

3.6 I-V characterization of Cu/ $Cu_{1-x}Zn_xFe_2O_4$ / p-Si Schottky barrier diodes with light variation

Fig. 12 shows the schematic diagram of Cu/ $Cu_{1-x}Zn_xFe_2O_4$ /p-Si MIS structured SBD. The I-V characteristics of Cu/ $Cu_{1-x}Zn_xFe_2O_4$ /p-Si type SBDs measured using Keithley source meter 2450 observed under dark and light conditions in the voltage range − 5 V to 5 V by varying the power of UV- C light sources are shown in Fig. 13. The diode under illumination shows higher values of current compared to dark indicating the photo-conducting nature of the fabricated diodes [55].

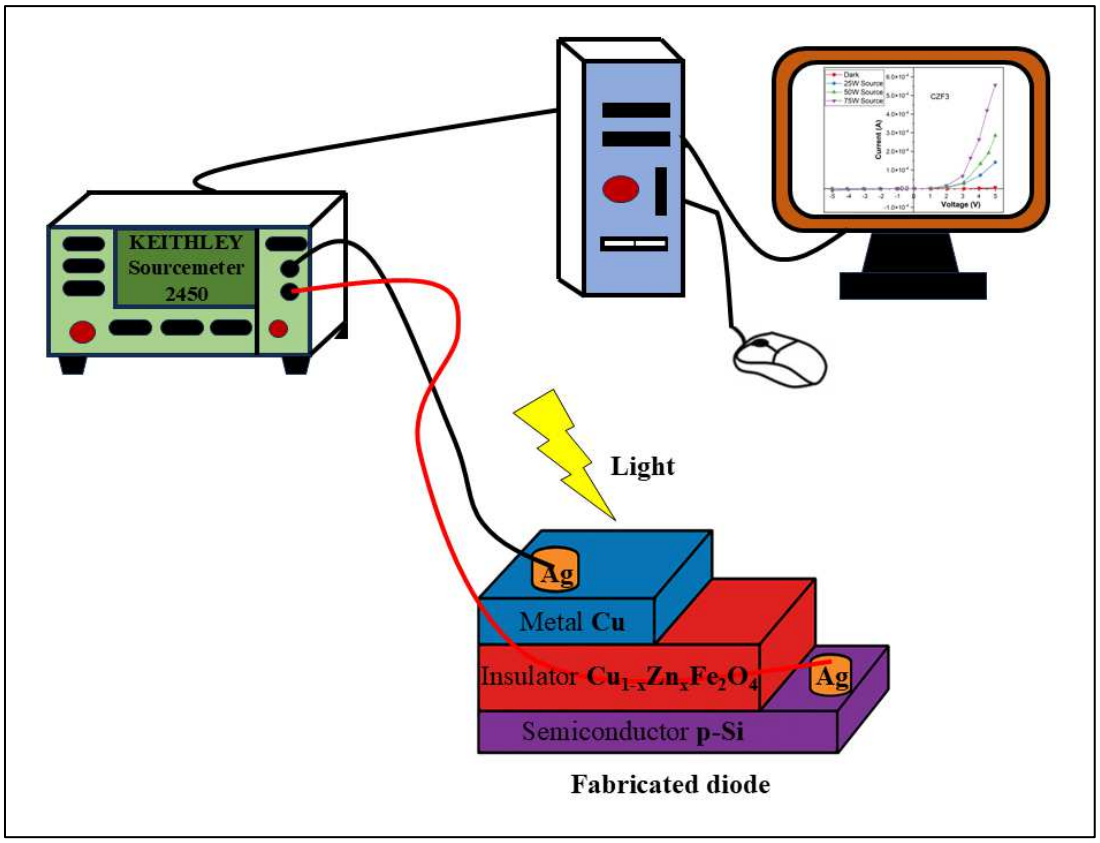


Fig. 12 Schematic diagram of Cu/ $Cu_{1-x}Zn_xFe_2O_4$ /p-Si MIS structured SBD

The increased current in an MIS diode upon illumination is a result of the photon induced charge carrier generation and the modification of the device's electrical characteristics, that is heavily influenced by the insulating layer which traps or accumulate charge carriers [56]. Also, the current increases with the illuminating power in all the fabricated diodes. When the illuminating power increases, a higher number of photons are incident on the MIS diode. A greater number of incident photons leads to a proportional increase in the generation of electron-hole pairs that directly contributes to a high photocurrent [57]. Ghamdi et. al [58] fabricated Al/WO_3/p-Si type photodiode and analyzed the photo conducting behaviour by varying illuminating power. He observed the increment in the current with the illuminating power in the fabricated diode.

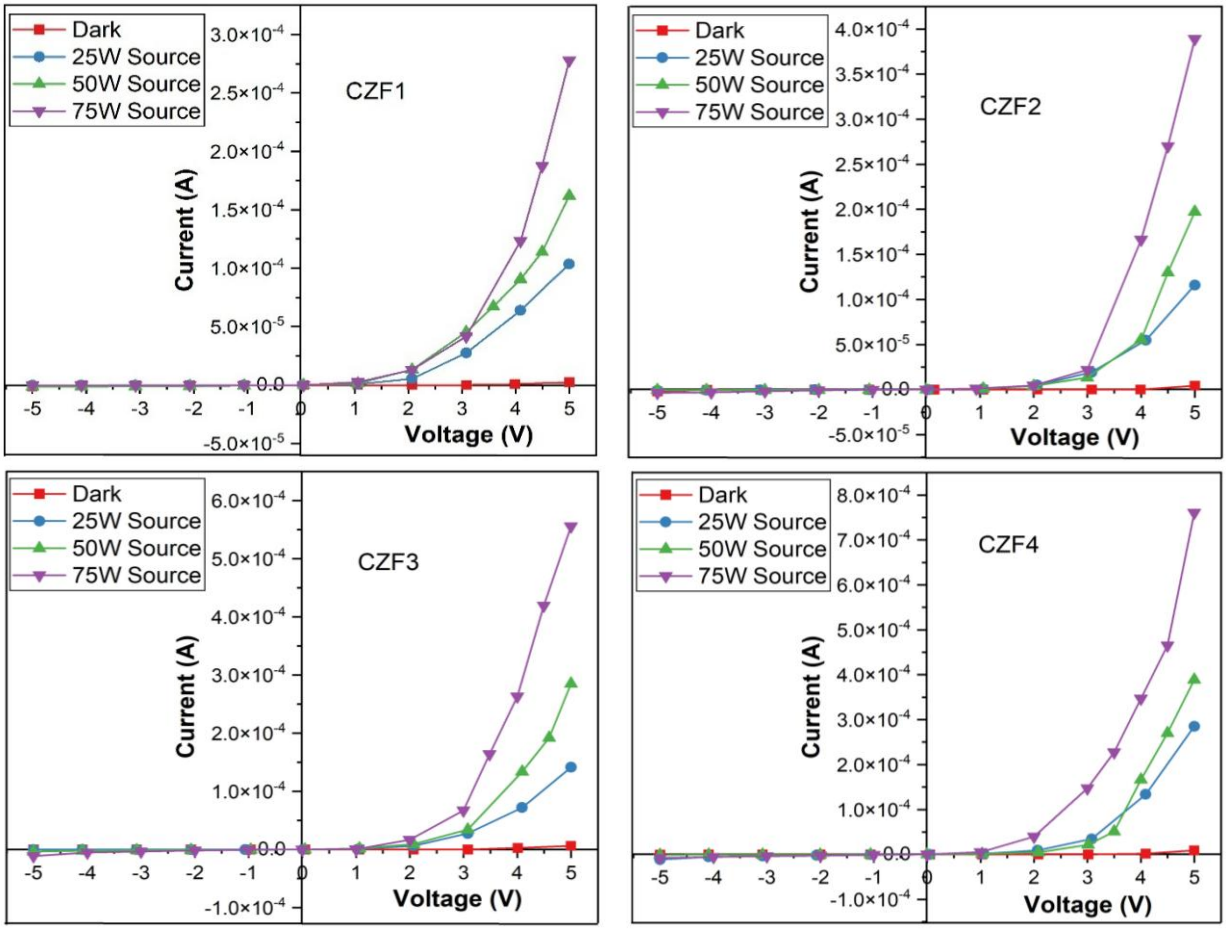


Fig. 13 Light dependent I–V characteristics of Cu/ $Cu_{1-x}Zn_xFe_2O_4$ /p-Si type SBDs

The ln (J)–V plot for Cu/ $Cu_{1-x}Zn_xFe_2O_4$ / p-Si type SBDs is shown in the Fig. 14. The current density (J) is calculated by considering the thermionic emission theory (TET) and the equation is given by [59]

$$J = J_0\left[\exp\left(\frac{qV}{nk_BT}\right) - 1\right] \tag{11}$$

$$J_0 = A^*T^2 \exp\left(-\frac{q\Phi_B}{k_BT}\right) \tag{12}$$

Where J_0, k_B, V, T, q, n, A* and Φ_B are reverse leakage current density, Boltzmann's constant, voltage, temperature in kelvin, electron charge, ideality factor, Richardson constant and barrier height. The ideality factor (n) and barrier height (Φ_B) are calculated using the following equations [60]

$$n = \frac{q}{k_BT}\left(\frac{d(V)}{d(\ln(J))}\right) \tag{13}$$

$$\Phi_B = \frac{k_BT}{q}\ln\left(\frac{A^*T^2}{J_0}\right) \tag{14}$$

The ideality factor characterizes the closeness of diode's behavior with the ideal diode equation. The ideal behaviour is characterized by an ideality factor of 1 [61]. Values greater than 1 indicate the non-ideal current-voltage characteristics of the diode and it arises due to the existence of a large number of trapping states, high density of interface states at M-S interface, barrier inhomogeneity, voltage drop at the insulating layer, bias-dependent barrier height and series resistance [62]. The ideality factor (n) of the diodes decreases with the increase in the illumination

power due to the production of a large number of electron-hole (e^- - h^+) pairs after the absorption of the light [63]. This behaviour is related to the photo conducting nature of the fabricated diodes. The diode having higher Zn concentration (CZF4) exhibits the lowest n value of 3.23 under illumination using 75 W source. CZF4 absorbs more photons to generate more charge carriers that crosses the higher junctions as indicated by absorption spectra also. The barrier height values of the diodes increase under illumination compared to dark conditions [64]. The surface of a semiconductor material has energy states that can trap the charges and the illumination changes the charge distribution within the depletion region thereby affecting the barrier height [65]. Fig. 15 depicts the Energy band diagram of the fabricated Cu/ $Cu_{1-x}Zn_xFe_2O_4$ /p-Si type SBDs.

To analyze the behaviour of the Cu/ $Cu_{1-x}Zn_xFe_2O_4$ /p-Si MIS diodes under variable illumination, the photodiode parameters like Photosensitivity (Ps), Responsivity (R), Quantum efficiency (QE) and Detectivity (D) are calculated using the following equations [60]

$$P_S = \frac{I_{Ph} - I_D}{I_D} \quad (15)$$

$$R = \frac{I_{Ph}}{PA} \quad (16)$$

$$QE = \frac{Rhc}{q\lambda} \quad (17)$$

$$D = \frac{R}{\sqrt{2qI_D}} \quad (18)$$

Where I_{Ph}, I_D, c, q, A, P, λ and h are photocurrent, dark current, velocity of light, electronic charge, area of the diode, optical power of the light, wavelength of light and Planck's constant. The evaluated diode parameters are recorded in the Table. 4.

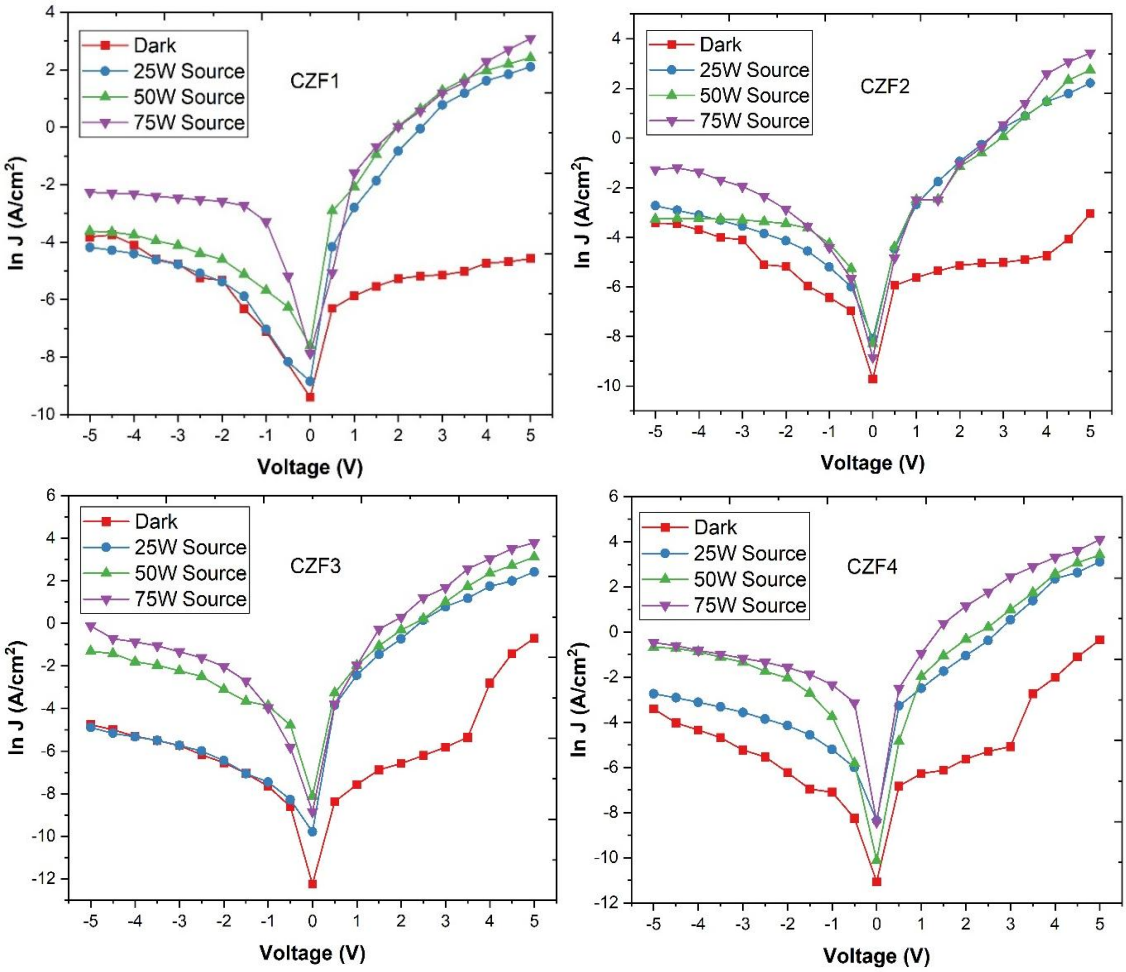


Fig. 14 Light dependent plots of ln (J)–V for Cu/ $Cu_{1-x}Zn_xFe_2O_4$ / p-Si type SBDs

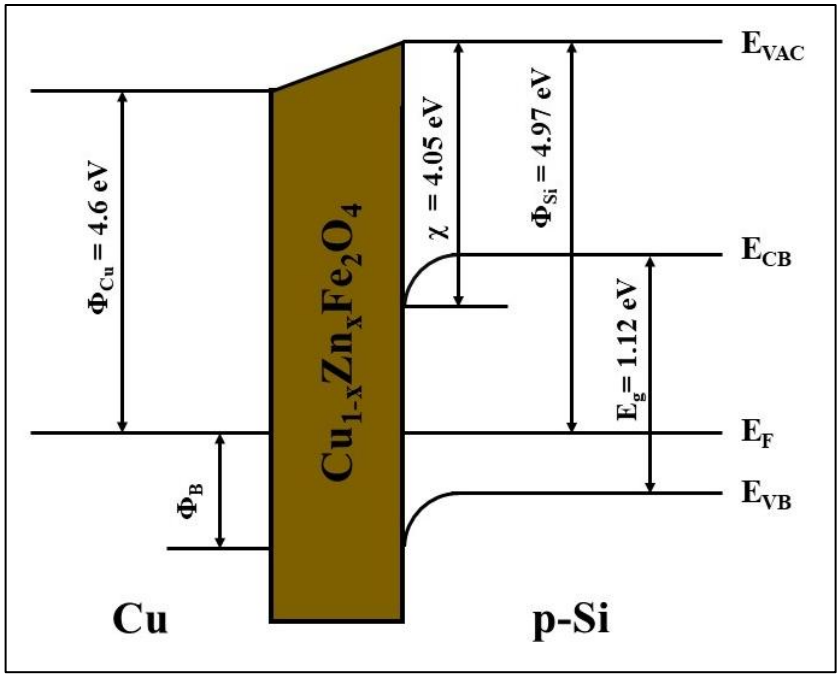


Figure. 15 Energy band diagram of Cu/ $Cu_{1-x}Zn_xFe_2O_4$ /p-Si type SBDs

Sample	Power of the light source (W)	Ideality factor (n)	Barrier height (eV)	Photo sensitivity (%)	Responsivity (mA/W)	Quantum efficiency (%)	Detectivity ($x10^{10}$) (Jones)
CZF1	0	5.84	0.634	-	-	-	-
	25	5.45	0.644	18000	10.6	4.12	3.86
	50	5.19	0.657	29600	15.9	6.16	6.11
	75	5.02	0.659	35100	23.2	8.99	7.80
CZF2	0	5.50	0.644	-	-	-	-
	25	5.32	0.651	17500	9.92	3.85	4.11
	50	4.93	0.659	25700	13.9	5.38	6.10
	75	4.77	0.660	35200	28.8	11.2	8.74
CZF3	0	4.94	0.653	-	-	-	-
	25	4.09	0.659	27300	12.6	4.90	4.20
	50	3.94	0.662	38700	23.6	9.17	6.66
	75	3.78	0.666	68600	48.6	18.8	12.6
CZF4	0	4.51	0.661	-	-	-	-
	25	3.77	0.668	32200	23.1	8.97	7.91
	50	3.62	0.676	41500	28.8	11.2	10.5
	75	3.23	0.688	106000	65.9	25.5	24.1

Table. 4 Diode parameters of Cu/ $Cu_{1-x}Zn_xFe_2O_4$ / p-Si SBDs

The photo-sensitivity of the fabricated diodes increases with illuminating power due to the production of electron-hole pair after light absorption [66]. CZF4 shows higher sensitivity making it an appropriate candidate for designing highly sensitive optoelectronic devices. R. Marnadu et. al [67] fabricated Cu/ Ce-WO_3/ p-Si diodes by varying intensity of light from 0 to 130mW/cm^2 and a maximum photosensitivity of 17509.62% was observed in the MIS diode fabricated with 12 % of Ce when illuminated at 130 mW/cm^2. The CZF4 shows highest responsivity of 65.9 when illuminated by 75W light source. A higher photo responsivity indicates the ability of the photodetector to produce enough electrical output from a given amount of incident light [68]. The Quantum efficiency (QE) is the number of charge carriers needed to produce the photocurrent for every photon incident on the device [69]. The maximum QE of 25.5 is shown by CZF4 under illumination using the 75W light source. This enhanced QE is due to the increased value of absorption coefficient of CZF4 film that is evident from the absorbance spectra. Increased photon absorption, separation and collection of the photogenerated charge carriers leads to high values of QE [70]. CZF4 has minimum band gap to support the penetration of higher energy photons to increase the QE. A maximal value of detectivity is shown by CZF4 so that it can be employed to detect even the weak signals ensuring the fabricated device can operate under low light conditions thereby maintaining high performance [71].

The enhanced device performance with increasing Zn concentration is attributed to the combined effect of (i) improved crystallinity, (ii) reduced lattice strain, and (iii) increased oxygen vacancy concentration, which introduce localized states near the conduction band. These states facilitate carrier transport via trap-assisted tunneling and reduce recombination losses. Consequently, improved charge separation and transport lead to enhanced responsivity and detectivity. The good agreement between the structural, morphological, optical and electrical studies defines a clear structure property-performance relationship, improved crystallinity, less lattice strain, uniform surface morphology and optimized oxygen vacancy concentration that collectively increase the transport at the $Cu_{1-x}Zn_xFe_2O_4$ / p-Si interface resulting in enhanced photodetection performance. The results show that interface engineering by composition provides a practical and scalable design of next generation ferrite-based MIS photodiodes. The fabricated Cu/ $Cu_{1-x}Zn_xFe_2O_4$ / p-Si SBDs (x=0.8) reveal a promising photo conducting behaviour that is very sensitive to light intensity indicating a strong potential for photodetector applications. The enhancement in photodiode performance with increasing Zn concentration cannot be attributed to a single structural parameter; rather, it results from the synergistic interaction between structural ordering, defect engineering and interface optimization. Larger crystallites reduce grain-boundary scattering, improved morphology enhances interface continuity, oxygen vacancies facilitate carrier transport, and the narrowed optical band gap increases photon absorption. These interconnected structural and electronic modifications collectively improve carrier generation, separation and extraction across the MIS junction, resulting in lower ideality factors, enhanced barrier homogeneity, higher responsivity and superior detectivity. The present study therefore establishes a clear structure–defect–interface–performance relationship for composition-engineered ferrite nano-interlayers.

3.7 I-V characterization of Cu/ $Cu_{1-x}Zn_xFe_2O_4$ / p-Si Schottky barrier diodes with temperature variation

Fig. 16 shows the I-V characteristics of the diodes recorded using Keithley source meter 2450 by varying temperature from 30˚C to 100˚C in the voltage range − 5 V to 5 V and studied how diode parameters are depending on the temperature. All devices preserve their rectifying behaviour throughout the investigated temperature range, demonstrating the excellent thermal stability of the $Cu_{1-x}Zn_xFe_2O_4$ nano interlayers and the robustness of the fabricated MIS junctions. The temperature dependent values of n and Φ_B are given in Table. 5.

The absence of abnormal current fluctuations further indicates the formation of stable and electrically homogeneous interfaces. There is an increment in the values of barrier height and decrement in the ideality factor with increment in the diode temperature emphasizing the role of interfacial layer to accomplish temperature-dependent performance [72]. The ln J versus V plot for Cu/ $Cu_{1-x}Zn_xFe_2O_4$ / p-Si SBDs in the temperature range of 30–100˚C are shown in Fig. 17. For CZF4, the ideality factor decreased to 4.08 at 100˚C suggesting enhanced electrical characteristics [73].

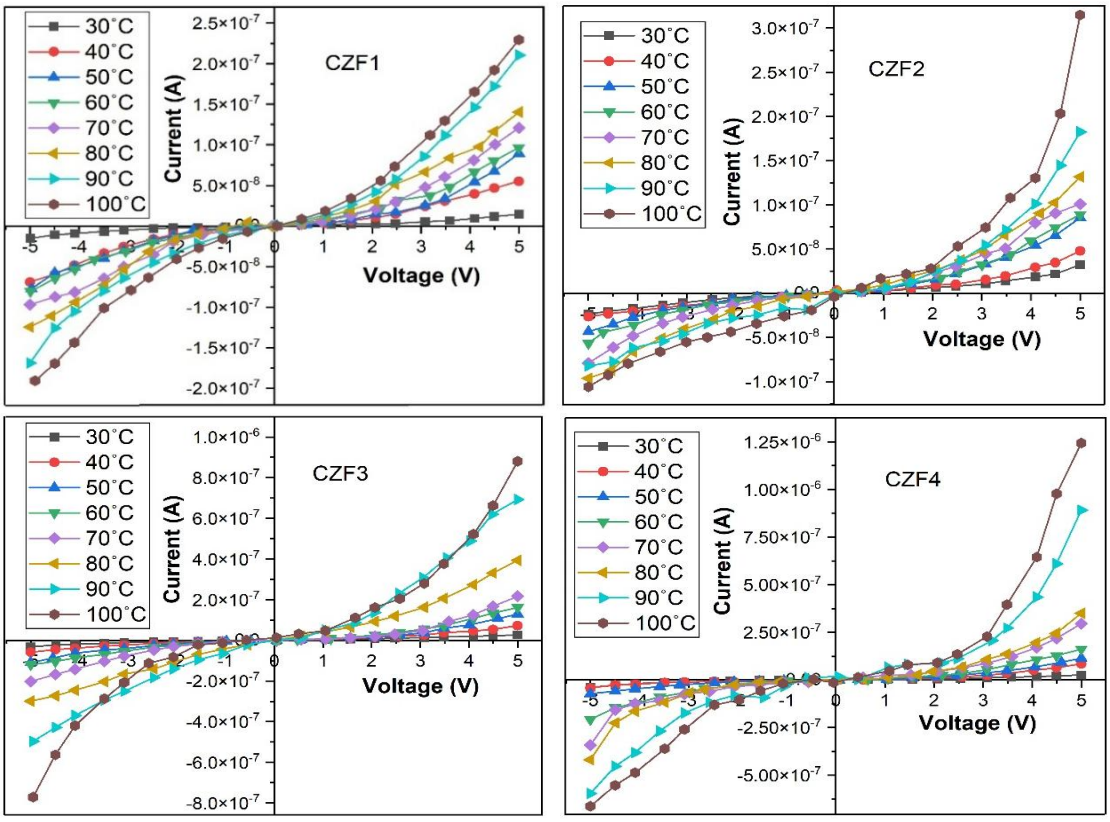


Fig. 16 I–V characteristics of the Cu/ $Cu_{1-x}Zn_xFe_2O_4$ / p-Si SBDs at different temperatures

As the ideality factor is not constant with temperature and the decrement in the value of n with temperature is observed, the existence of a temperature-dependent charge transport mechanism can be confirmed [74]. The presence of the $Cu_{1-x}Zn_xFe_2O_4$ layer influences the charge recombination processes thereby improving the rectification behaviour and diode performance [75]. The electrons at low temperatures can overcome the lower barriers as the current transport across the metal–semiconductor interface is a temperature activated process [76]. As the temperature and bias increases, more and more electrons acquire enough energy to overcome the higher barrier leading to increased barrier height with temperature [77]. The increase in barrier height and the simultaneous decrease in ideality factor with increasing temperature suggest progressive activation of thermionic emission and improved barrier homogeneity. Such behaviour has been reported in recent MIS Schottky photodiodes employing engineered oxide interlayers, where temperature facilitates carrier transport across a more uniform interface while reducing the influence of localized interface states. The temperature dependence of the ideality factor and barrier height for Cu/ $Cu_{1-x}Zn_xFe_2O_4$ / p-Si SBDs is shown in Fig. 18. A. Tataroˇglu et.al [72] analyzed the current–voltage (I–V) characteristics of Au/SiO_2/n-Si (MIS) Schottky diodes in the temperature range of 300–400K and observed a decrease in the value of n and an increase in Φ_B with increasing temperature. Mehmet Okan Erdal et. al [78] analyzed the I-V characteristics of Al/TiO_2/n-Si SBDs in the temperature range of 50K– 400K and the strong dependence of diode parameters on temperature is observed. The n decreases and Φ_B increases with increasing temperature. The enhanced thermal response shows that the composition-controlled interface engineering will not only improve the device performance at room temperature but also ensure the stable operation under various environmental conditions.

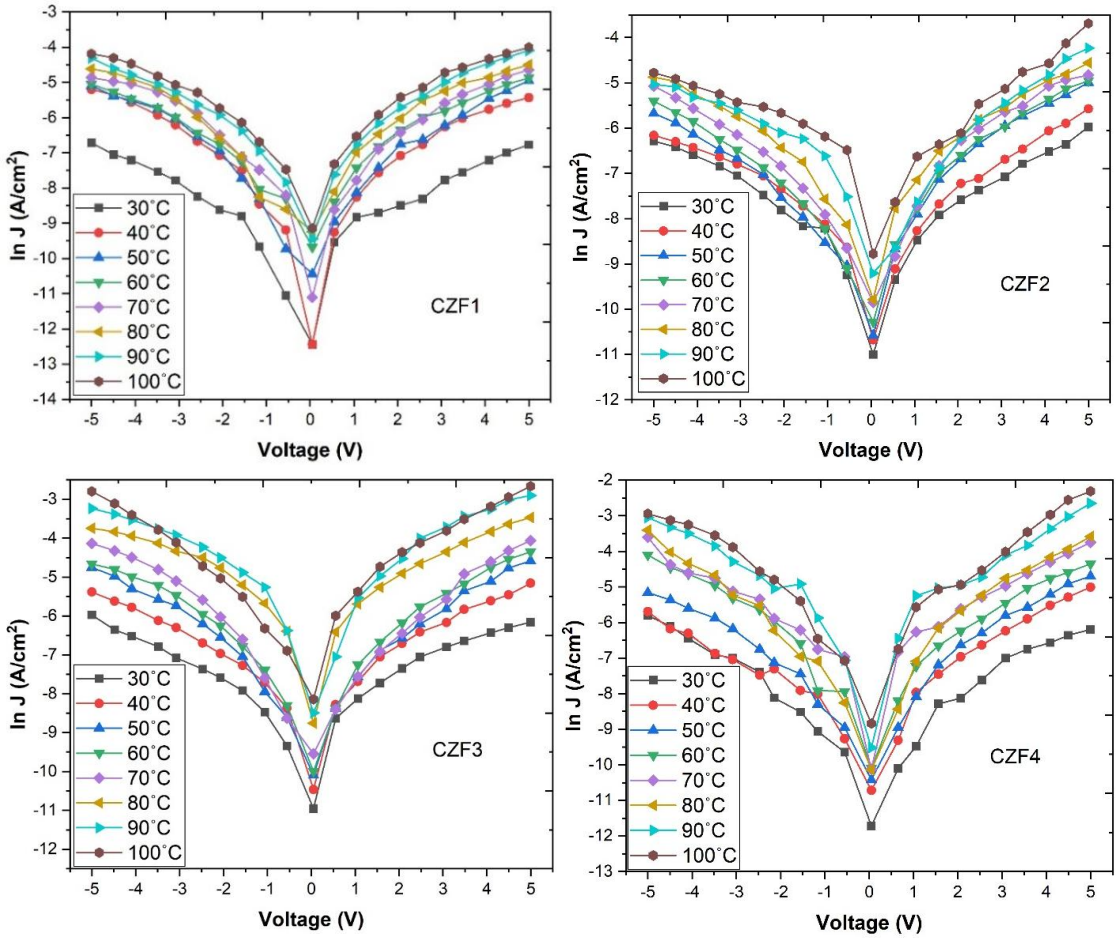


Fig. 17 Temperatures dependent ln (J)–V plots for Cu/ $Cu_{1-x}Zn_xFe_2O_4$ / p-Si SBDs

Temperature (℃)	Ideality factor (n)				Barrier height eV (Φ_B)			
	CZF1	CZF2	CZF3	CZF4	CZF1	CZF2	CZF3	CZF4
30	6.19	5.98	5.71	5.68	0.642	0.644	0.646	0.648
40	6.02	5.75	5.42	5.14	0.646	0.649	0.651	0.653
50	5.82	5.58	5.26	5.02	0.648	0.651	0.655	0.658
60	5.35	5.24	5.12	4.94	0.651	0.653	0.659	0.664
70	5.17	5.01	4.83	4.64	0.657	0.658	0.661	0.668
80	5.01	4.87	4.51	4.35	0.661	0.666	0.669	0.670
90	4.90	4.68	4.34	4.23	0.665	0.670	0.671	0.673
100	4.74	4.57	4.30	4.08	0.668	0.675	0.678	0.680

Table. 5 Diode parameters of Cu/ $Cu_{1-x}Zn_xFe_2O_4$ / p-Si SBDs at different temperatures

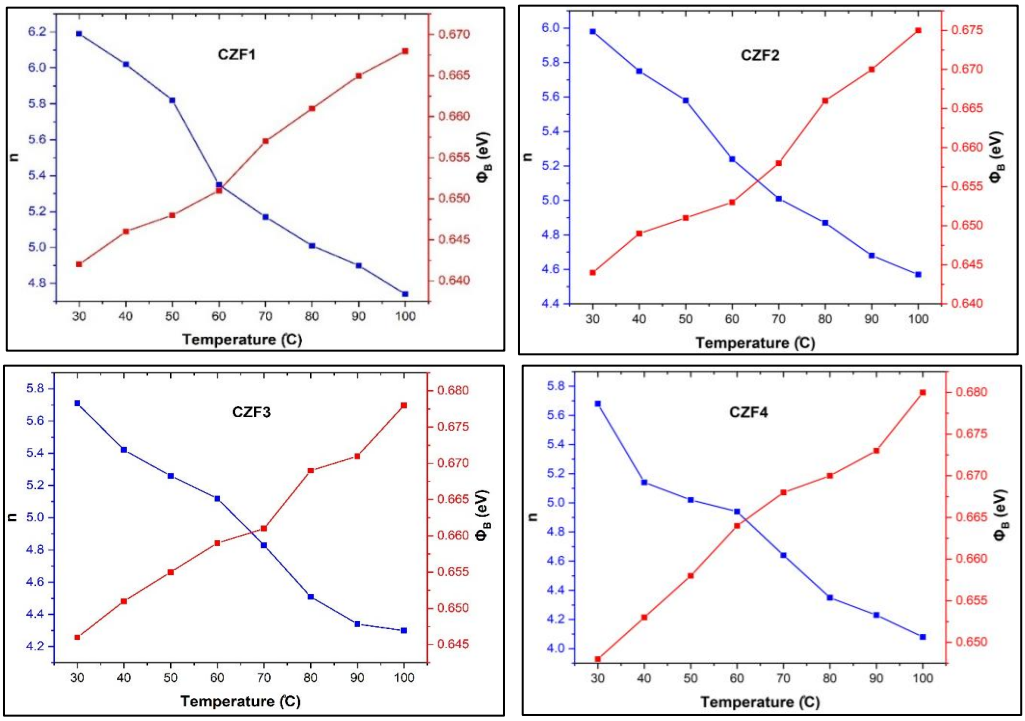


Fig. 18 Temperature dependent variation of n and Φ_B for Cu/ $Cu_{1-x}Zn_xFe_2O_4$ / p-Si SBDs

3.8 Capacitance – Voltage (C-V) characteristics of Cu/ $Cu_{1-x}Zn_xFe_2O_4$ / p-Si diodes

The C-V characteristics of Cu/ $Cu_{1-x}Zn_xFe_2O_4$ / p-Si diodes at room temperature recorded using Keysight E4990A impedance analyzer is shown in Fig. 19. A high frequency of 1 MHz is used for studying CV profile due to the minimal contribution to capacitance from interface traps at high frequency. The comparatively flat curves with weak voltage dependence imply uniform charge distribution in the material, stable dielectric response under bias and minimal interface states or traps. The nearly constant capacitance over the voltage range indicates good electrical stability and low interface defect density. The enhanced carrier injection or charge accumulation causes a small increase in capacitance at positive bias [79]. It is clear that CZF4 shows the highest capacitance and CZF1 the lowest. This increase is due to the higher dielectric constant due to better crystallinity, increased polarization and reduced defects that enhances charge storage ability.

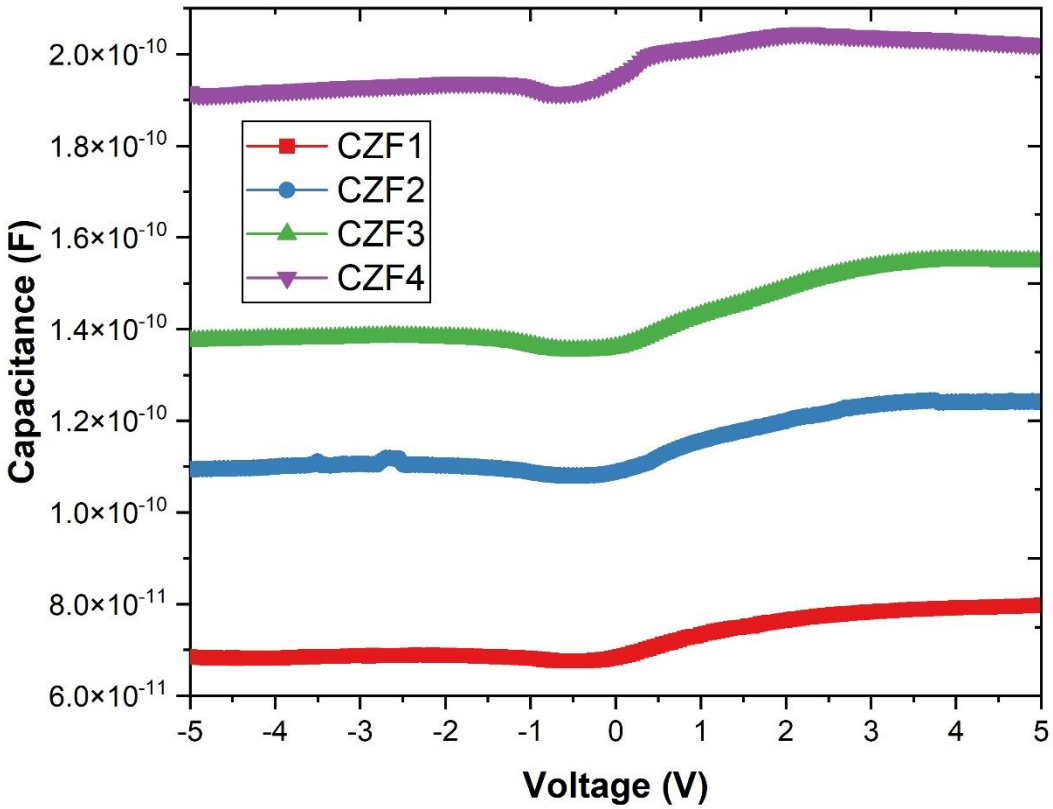


Fig. 19 C-V characteristics of Cu/ $Cu_{1-x}Zn_xFe_2O_4$ / p-Si diodes

Fig. 20 shows the C^{-2}-V plot from where barrier height can be evaluated using the following equation [80]

$$\Phi_B = V_d + \frac{kT}{q} \ln\left(\frac{N_d}{N_c}\right) \quad (19)$$

V_d is the diffusion potential, N_d is calculated from the slope of C^{-2}-V plot. The origin of kT/q term is by the penetration of electrons from the metal to the depletion region [81]. $N_c=2.8\times10^{19}cm^3$ is the effective density of states in Si conduction band. The parameters obtained from C^{-2}-V characteristics are given in Table. 6. The comparison of the performance parameters of Cu/ $Cu_{1-x}Zn_xFe_2O_4$ / p-Si diode with previous reports are summarized in Table. 7. The optimized Cu/CZF4/p-Si photodiode shows the maximum built-in potential along with favorable depletion characteristics, indicating the superior quality of the composition engineered interface.

Sample	V_d (V)	N_d (cm^{-3})	Φ_B (I-V method) (eV)	Φ_B (C-V method) (eV)
CT4	1.45	1.94×10^{19}	0.642	0.427
CT6	1.60	6.42×10^{18}	0.644	0.487
CT8	1.81	3.56×10^{18}	0.646	0.669
CT10	1.94	1.49×10^{18}	0.648	0.710

Table. 6 The parameters obtained from C^{-2}-V characteristics of Cu/ $Cu_{1-x}Zn_xFe_2O_4$ /p-Si SBDs

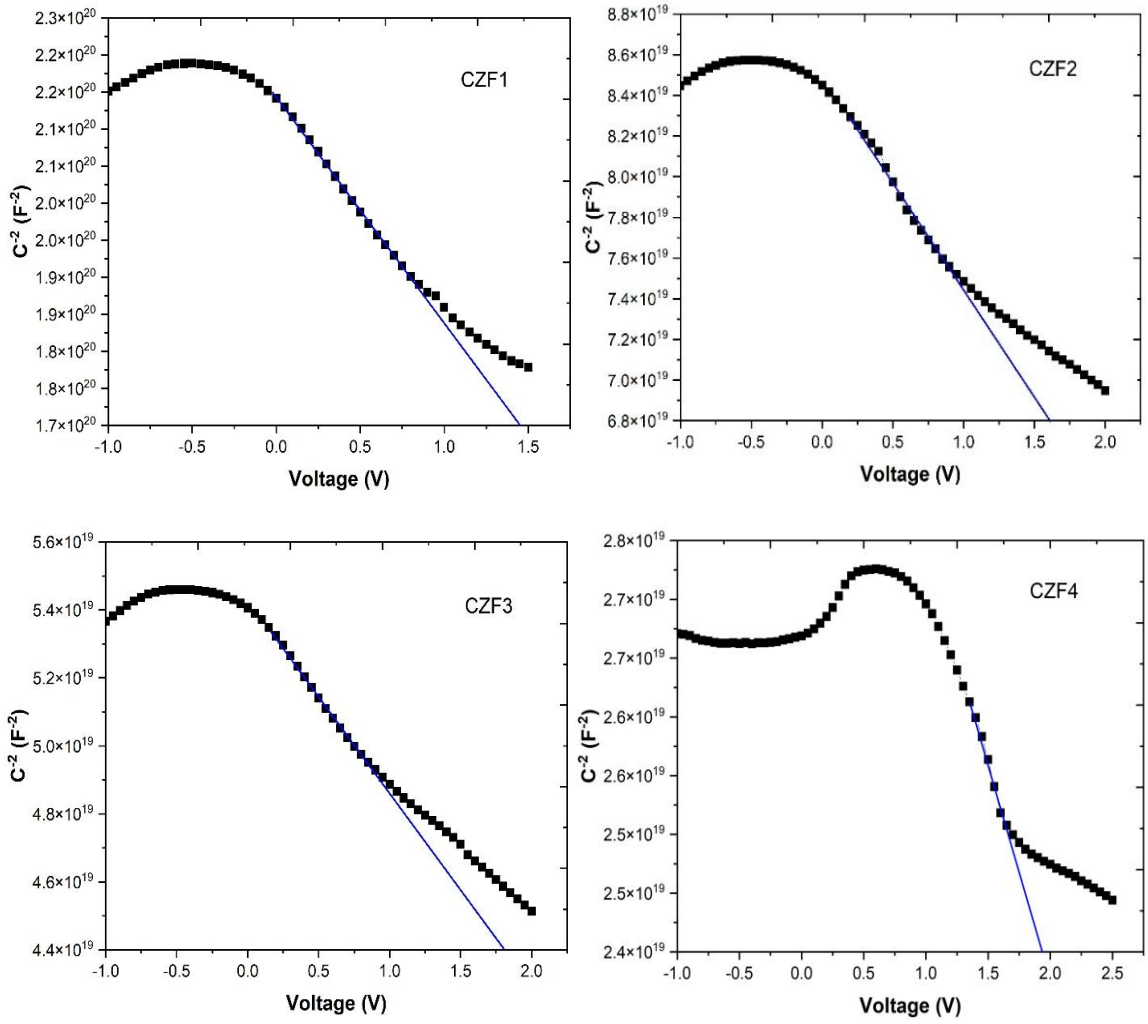


Fig. 20 C^{-2}-V plots of Cu/ $Cu_{1-x}Zn_xFe_2O_4$ / p-Si diodes

Author	Device structure	Photosensitivity (%)	Responsivity (mA/W)	Quantum efficiency (%)	Detectivity (Jones)
Vivek et.al [82]	Cu/MoO_3/p-Si	610.51	35.130	136.22	11.49 x10^{10}
G. Su et.al [83]	SnS_2/SiO_2/Si	-	8.8	2.4	2 x10^9
V. Balasubramani et.al [84]	Cu/Yb@V_2O_5/n-Si	75545.70	37.90	25.93	9.97 x10^{10}
S. Sil et.al [85]	Al/Cu_5FeS_4/FTO	1.13	1.52	-	2.77 x10^{10}
R. Marnadu et.al [86]	Cu/Sn-WO_3/p-Si	960.95–137.63	5083.5	1971.1	12.089 x10^{10}

P. Gayathri et.al [87]	Cu/ZrO_2@Zn/n-Si	10151.51	2.95 x10^{-4}	1.14 x10^{-3}	1.17 x10^{9}
V. Balasubramani et.al [88]	Cu/Nd-V_2O_5/n-Si	19427.80	23.79	14.10	-
B. Zu et.al [89]	Au/SiO_2/Si	-	0–4.5	0.27-0.71	1.01- 1.50 x10^{10}
Present work	Cu/$Cu_{1-x}Zn_xFe_2O_4$ / p-Si	18000-106000	10.6-65.9	4.12-25.5	3.86-24.1 x10^{10}

Table. 7 Comparison of the Cu/ $Cu_{1-x}Zn_xFe_2O_4$ / p-Si diode performance with previous reports

Overall, the present investigation demonstrates that Zn substitution serves as an effective composition-controlled defect engineering approach rather than merely compositional modification. Structural ordering, defect chemistry, optical absorption and interface quality evolve simultaneously with increasing Zn concentration, producing a synergistic improvement in charge transport across the MIS junction. This comprehensive correlation between crystal structure, oxygen vacancy concentration, interface quality and photodetection characteristics provides valuable design guidelines for developing next-generation ferrite-based silicon-compatible optoelectronic devices.

4. Conclusions

This work establishes that composition-controlled defect and interface engineering is an effective strategy for improving the performance of ferrite-based MIS photodiodes. Zn substitution simultaneously enhances crystallinity, reduces lattice strain, optimizes oxygen-vacancy concentration, improves interface quality and facilitates efficient carrier transport across the $Cu_{1-x}Zn_xFe_2O_4$/p-Si junction. The systematic correlation established between structural evolution, defect chemistry, optical properties and electrical performance provides fundamental insight into the structure–defect–interface–performance relationship governing ferrite nano-interlayers. The optimized composition $Cu_{0.2}Zn_{0.8}Fe_2O_4$ MIS diode sample (CZ4) exhibits superior photodiode characteristics, including low ideality factor, high responsivity, enhanced quantum efficiency and high detectivity under illumination. The improved performance is attributed to defect-mediated charge transport, enhanced crystallinity, and improved interface quality. The strong dependence of diode parameters on both light intensity and temperature highlights the multifunctional nature of the device. The results confirm that Zn-induced interface engineering plays a decisive role in tailoring charge transport and enhancing the optoelectronic performance of MIS Schottky diodes. The demonstrated facile chemical bath deposition, composition-tunable nano interlayers and excellent ultraviolet photodetection performance suggest that $Cu_{1-x}Zn_xFe_2O_4$ is a promising interfacial material for next-generation silicon compatible optoelectronic devices. Future work may involve optimizing the film thickness, extending the spectral response to the visible region through further compositional engineering and incorporating these MIS photodiodes into flexible self-powered and wearable sensing platforms for environmental monitoring, biomedical diagnostics and optical communication.

Statements and Declarations

Funding

The authors declare that no funds, grants, or other support were received during the preparation of this manuscript.

Competing interests

The authors have no relevant financial or non-financial interests to disclose.

Authors' contributions

All authors whose names appear on the submission made substantial contributions to the conception or design of the work; or the acquisition, analysis, or interpretation of data; or the creation of new software used in the work; drafted the work or revised it critically for important intellectual content; approved the version to be published; and agree to be accountable for all aspects of the work in ensuring that questions related to the accuracy or integrity of any part of the work are appropriately investigated and resolved.

Data Availability

The datasets generated during and/or analysed during the current study are available from the corresponding author on reasonable request.

Acknowledgement

The authors acknowledge UGC, DST-FIST and KSCSTE for the support in setting up of facilities for research at Sree Kerala Varma College, Thrissur. Author Aiswarya K U likes to thank Kerala State Council for Science Technology and Environment (KSCSTE), Government of Kerala for awarding a research fellowship grant.

References

1. Venkatesan, Arumugam, Nagamuthu Raja Krishna Chandar, Arumugam Kandasamy, Madhu Karl Chinnu, Kalasalingam Nagappan Marimuthu, Rangasamy Mohan Kumar, Ramasamy Jayavel (2015) Luminescence and electrochemical properties of rare earth (Gd, Nd) doped V_2O_5 nanostructures synthesized by a non-aqueous sol–gel route. RSC Advances 5, no. 28: 21778-21785. https://doi.org/10.1039/C4RA14542A.
2. Zhang, W., Y. Cui, Z. G. Hu, W. L. Yu, J. Sun, N. Xu, Z. F. Ying, J. D. Wu (2012) Structural, optical and electrical properties of high-k ZrO_2 dielectrics on Si prepared by plasma assisted pulsed laser deposition. Thin Solid Films 520, no. 20: 6361-6367. https://doi.org/10.1016/j.tsf.2012.06.042.
3. Badali, Yusuf, Yashar Azizian-Kalandaragh, İbrahim Uslu, Şemsettin Altindal (2020) Investigation of the effect of different Bi_2O_3– x: PVA (x= Sm, Sn, Mo) thin insulator interface-layer materials on diode parameters. Journal of Materials Science: Materials in Electronics 31: 8033-8042. https://doi.org/10.1007/s10854-020-03343-5.
4. Aiswarya K. U, Arun, K. J, M. D. Aggarwal (2024) Fabrication and characterization of illumination-dependent Cu/p-Si Schottky barrier diodes with P(VDF-TrFE)-Ho_2O_3 nano composite as interfacial insulating layer. Emergent Materials: 1-12. https://doi.org/10.1007/s42247-024-00897-6.
5. Naama, S., T. Hadjersi, A. Keffous, G. Nezzal (2015) CO_2 gas sensor based on silicon nanowires modified with metal nanoparticles. Materials Science in Semiconductor Processing 38: 367-372.

https://doi.org/10.1016/j.mssp.2015.01.027.

6. Vittal R, Kuo-Chuan Ho (2017) Zinc oxide-based dye-sensitized solar cells: A review. Renewable and Sustainable energy reviews 70: 920-935. https://doi.org/10.1016/j.rser.2016.11.273.
7. Dökme, İlbilge, Tuncay Tunç, İbrahim Uslu, Şemsettin Altındal (2011) The Au/polyvinyl alcohol (Co, Zn-doped)/n-type silicon Schottky barrier devices. Synthetic metals 161, no. 5-6: 474-480. https://doi.org/10.1016/j.synthmet.2011.01.002.
8. Kumar, E. Ranjith, R. Jayaprakash, G. Sarala Devi, P. Siva Prasada Reddy (2014) Synthesis of Mn substituted $CuFe_2O_4$ nanoparticles for liquefied petroleum gas sensor applications. Sensors and Actuators B: Chemical 191: 186-191. https://doi.org/10.1016/j.snb.2013.09.108.
9. Hyeon, Taeghwan, Yunhee Chung, Jongnam Park, Su Seong Lee, Young-Woon Kim, Bae Ho Park (2002) Synthesis of highly crystalline and monodisperse cobalt ferrite nanocrystals. The Journal of Physical Chemistry B 106, no. 27: 6831-6833. https://doi.org/10.1021/jp026042m.
10. Dionne, Gerald F., Daniel E. Oates, Donald H. Temme, Jerald A. Weiss (2002) Ferrite-superconductor devices for advanced microwave applications. IEEE Transactions on Microwave theory and Techniques 44, no. 7: 1361-1368. https://doi.org/10.1109/22.508241.
11. Yin, H., P. S. Casey, G. M. Chow (2012) Nanocrystalline nickel ferrite particles synthesized by non-hydrolytic sol–gel method and their composite with biodegradable polymer. Journal of Nanoscience and Nanotechnology 12, no. 11: 8431-8436. https://doi.org/10.1166/jnn.2012.6682.
12. Mujasambatoo, Khalid, Shalendra Kumar, M. Shahnawaze Ansari (2011) Ferrimagnetic ordering of Ti^{4+} doped $Mn_{1+x}Fe_{2-2x}O_4$ ($0 \leq x \leq 0.5$) ferrites at room temperature. Science of Advanced Materials 3, no. 1: 120-126. https://doi.org/10.1166/sam.2011.1143.
13. Bhattacharya, Sanjib, Tanusree Kar, Arun Kr Bar, Debasish Roy, M. P. F. Graca, M. A. Valente (2011) Structural behaviors and optical properties of semiconducting zinc-molybdate glass nanocomposites. Science of Advanced Materials 3, no. 2: 284-288. https://doi.org/10.1166/sam.2011.1158.
14. Bellucci, F. S., L. O. Salmazo, E. R. Budemberg, M. R. Da Silva, M. A. Rodríguez-Pérez, Marcos Augusto Lima Nobre, Aldo Eloizo Job (2012) Preparation and structural characterization of vulcanized natural rubber nanocomposites containing nickel-zinc ferrite nano powders. Journal of Nanoscience and Nanotechnology 12, no. 3: 2691-2699. https://doi.org/10.1166/jnn.2012.5694.
15. Krishna, Rahul, Elby Titus, Sudeshna Chandra, Neel Kanth Bardhan, Rohit Krishna, Dhirendra Bahadur, José Gracio (2012) Fabrication of a glucose biosensor based on citric acid assisted cobalt ferrite magnetic nanoparticles. Journal of Nanoscience and Nanotechnology 12, no. 8: 6631-6638. https://doi.org/10.1166/jnn.2012.4570.
16. Arulmurugan, R., G. Vaidyanathan, S. Sendhilnathan, B. Jeyadevan (2006) Mn–Zn ferrite nanoparticles for ferrofluid preparation: Study on thermal–magnetic properties. Journal of magnetism and magnetic materials 298, no. 2: 83-94. https://doi.org/10.1016/j.jmmm.2005.03.002.

17. Aiswarya, K. U., K. J. Arun, M. D. Aggarwal (2025) Wet Chemical Synthesis Optimisation and Characterisation of Nano Holmium Oxide for Photocatalytic and Dielectric Device Applications. Surface Engineering and Applied Electrochemistry 61, no. 1: 12-23. https://doi.org/10.3103/S1068375524700522.
18. Mathew, Daliya S., Ruey-Shin Juang (2007) An overview of the structure and magnetism of spinel ferrite nanoparticles and their synthesis in microemulsions. Chemical engineering journal 129, no. 1-3: 51-65. https://doi.org/10.1016/j.cej.2006.11.001.
19. Abdeen, A. M. (1998) Electric conduction in Ni–Zn ferrites. Journal of magnetism and magnetic materials 185, no. 2: 199-206. https://doi.org/10.1016/S0304-8853(97)01144-X.
20. J. Slama, A. Gruskova, M. Usakova, E. Usak, R. Dosoudil (2009) Analysis of Cu-Substituted Ni Zn ferrites. J. Magn. Magn Mater 321: 3346–3351. https://doi. org/10.1016/j.jmmm.2009.06.024.
21. M.A. Ahmed, A.A.I. Khalil, S. Solyman (2007) Laser induced structural and transport properties change in Cu-Zn ferrites. J. Mater. Sci 42: 4098–4109. https:// doi.org/10.1007/s10853-006-1151-z.
22. S.A. Mazen, M.A. Ahmed, B.A. Sabra (1982) Thermal studies on the electrical conduction mechanism of $CuFe_2O_4$. Phys. Status Solidi. 70: K71–K75. https:// doi.org/10.1002/pssa.2210700158, 141.
23. M.C. Dimri, A.K. Verma, S.C. Kashyap, D.C. Dube, O.P. Thakur (2006) Structural, dielectric and magnetic properties of NiCuZn ferrite grown by citrate precursor method. Mater. Sci. Eng. B 133: 42–48. https://doi.org/10.1016/j.mseb. 2006.04.043.
24. A. Verma, T.C. Goal, R.G. Mendiratta, P. Kishan (2000) Magnetic properties of nickel-zinc ferrites prepared by the citrate precursor method. J. Magn. Magn Mater 208: 13–19. https://doi.org/10.1016/S0304-8853(99)00585-5.
25. N. Nanba, S. Kobayashi (1978) Semiconductive properties and cation distribution of copper ferrites. Jpn. J. Appl. Phys 17: 1819–1823. https://doi.org/10. 1143/JJAP.17.1819.
26. B. Duong, S. Seraphin, P. Laokul, C. Masingboon, S. Maensiri (2008) Ni–Cu–Zn ferrite prepared by aloe vera plant extract or egg white. Microsc. Microanal 14: 326–327. https://doi.org/10.1017/S1431927608083839.
27. X. Zuo, A. Yang, C. Vittoria, V.G. Harris (2006) Computational study of copper ferrite ($CuFe_2O_4$). J. Appl. Phys 99: 2006–2010. https://doi.org/10.1063/1. 2170048.
28. C. Yao, Q. Zeng, G.F. Goya, T. Torres, J. Liu, H. Wu, M. Ge, Y. Zeng, Y. Wang, J.Z. Jiang (2007) $ZnFe_2O_4$ nanocrystals: synthesis and magnetic properties. J. Phys. Chem C 111: 12274–12278. https://doi.org/10.1021/jp0732763.
29. M.M. Rashad, R.M. Mohamed, M.A. Ibrahim, L.F.M. Ismail, E.A. Abdel-Aal (2012) Magnetic and catalytic properties of cubic copper ferrite nano powders synthesized from secondary resources. J. Adva. Powd. Techno 23: 315. https:// doi.org/10.1016/j.apt.2011.04.005.
30. Arun, K. J., K. Shijith Kumar, A. K. Batra, M. D. Aggarwal, P. J. Francis (2015) Surfactant free hydrothermal synthesis of CdO nanostructure and its characterization. Advanced Science, Engineering and Medicine 7, no. 9: 771-775. https://doi.org/10.1166/asem.2015.1755.

31. Rajesh, C., K. J. Arun (2021) Accelerated photodegradation of solid phase polystyrene by nano TiO_2-graphene oxide composite under ultraviolet radiation. Polymer Degradation and Stability 184: 109476. https://doi.org/10.1016/j.polymdegradstab.2020.109476.
32. Asha, K., K. J. Arun (2023) Facile synthesis optimization and characterization of zinc tungstate nano particles for scintillator applications. In AIP Conference Proceedings, vol. 2783, no. 1. AIP Publishing. https://doi.org/10.1063/5.0159021.
33. Najmoddin, Najmeh, Ali Beitollahi, Hüseyin Kavas, Seyed Majid Mohseni, Hamidreza Rezaie, Johan Åkerman, Muhammet S. Toprak (2014) XRD cation distribution and magnetic properties of mesoporous Zn-substituted $CuFe_2O_4$. Ceramics International 40, no. 2: 3619-3625. https://doi.org/10.1016/j.ceramint.2013.09.063.
34. Aiswarya, K. U., Arun, K. J., M. D. Aggarwal, R. Marnadu, Pius Augustine (2025) Dielectric studies, ferroelectric behaviour and electronic transport mechanisms in β phase enhanced P (VDF-TrFE)/Ho_2O_3 films for possible energy storage applications. Measurement: Energy 100046. https://doi.org/10.1016/j.meaene.2025.100046.
35. Raj, Nimisha Babu, K. J. Arun (2023) Hydrothermal synthesis of lead tungstate nanoparticles and its characterisation. In AIP Conference Proceedings, vol. 2783, no. 1. AIP Publishing. https://doi.org/10.1063/5.0159020.
36. Aiswarya, K. U., K. J. Arun, Mohan D. Aggarwal (2025) Calcination tuned structural, optical and dielectric properties of wet chemically synthesised Cadmium Tungstate nanoparticles for photocatalytic and photodetector applications. New Journal of Chemistry. https://doi.org/10.1039/D5NJ03272E.
37. Ahmed, Arham S., M. L. Singla, Sartaj Tabassum, Alim H. Naqvi, Ameer Azam (2011) Band gap narrowing and fluorescence properties of nickel doped SnO_2 nanoparticles. Journal of luminescence 131, no. 1: 1-6. https://doi.org/10.1016/j.jlumin.2010.07.017.
38. Hammad, Talaat M., Jamil K. Salem, Ayman Abu Amsha, Nasser K. Hejazy (2018) Optical and magnetic characterizations of zinc substituted copper ferrite synthesized by a co-precipitation chemical method. Journal of Alloys and Compounds 741: 123-130. http://dx.doi.org/10.1016/j.jallcom.2018.01.123.
39. Chen, Z. C., L. J. Zhuge, X. M. Wu, Y. D. Meng (2007) Initial study on the structure and optical properties of $Zn_{1-x}Fe_xO$ films. Thin Solid Films 515, no. 13: 5462-5465. https: //doi.org/10.1016/j.tsf.2007.01.015.
40. Wang, Y. S., P. John Thomas, P. O'Brien (2006) Optical properties of ZnO nanocrystals doped with Cd, Mg, Mn, and Fe ions. The Journal of Physical Chemistry B 110, no. 43: 21412-21415. https: //doi.org/10.1021/jp0654415.
41. Yogo, Toshinobu, Tomoko Nakafuku, Wataru Sakamoto, Shin-ichi Hirano (2005) Synthesis of Fe-doped ZnO particle/polymer hybrid from metalorganics. Journal of materials research 20, no. 6: 1470-1475. https://doi.org/10.1557/JMR.2005.0187.
42. Bera, Santanu, A. A. M. Prince, S. Velmurugan, P. S. Raghavan, R. Gopalan, G. Panneerselvam, S. V. Narasimhan (2001) Formation of zinc ferrite by solid-state reaction and its characterization by XRD and XPS. Journal of materials science 36, no. 22: 5379-5384. https://doi.org/10.1023/A:1012488422484.

43. Hsiang, Hsing-I., Chi-Shiung Hsi, Chi-Yao Tsai, Li-Then Mei (2015) Cobalt-substitution effects on dielectric properties of CuZn ferrites. Ceramics International 41, no. 3: 4140-4144. https://doi.org/10.1016/j.ceramint.2014.11.110.
44. Wang, Yuxian, Hongqi Sun, Ha Ming Ang, Moses O. Tadé, Shaobin Wang (2014) Facile synthesis of hierarchically structured magnetic $MnO_2/ZnFe_2O_4$ hybrid materials and their performance in heterogeneous activation of peroxymonosulfate. ACS applied materials & interfaces 6, no. 22: 19914-19923. https://doi.org/10.1021/am505309b.
45. Poulin, Suzie, R. França, L. Moreau-Bélanger, Edward Sacher (2010) Confirmation of X-ray photoelectron spectroscopy peak attributions of nanoparticulate iron oxides using symmetric peak component line shapes. The Journal of Physical Chemistry C 114, no. 24: 10711-10718. https://doi.org/10.1021/jp100964x.
46. Qin, Wenxiu, Guodong Fang, Yujun Wang, Dongmei Zhou (2018) Mechanistic understanding of polychlorinated biphenyls degradation by peroxymonosulfate activated with $CuFe_2O_4$ nanoparticles: Key role of superoxide radicals. Chemical Engineering Journal 348: 526-534. https://doi.org/10.1016/j.cej.2018.04.215.
47. Nair, Pooja Raveendran, Claudia Rosa Santiago Ramirez, Miguel Angel Gracia Pinilla, Bindu Krishnan, David Avellaneda Avellaneda, Rene Fabian Cienfuegos Pelaes, Sadasivan Shaji (2023) Black titanium dioxide nanocolloids by laser irradiation in liquids for visible light photo-catalytic/electrochemical applications. Applied Surface Science 623: 157096. https://doi.org/10.1016/j.apsusc.2023.157096.
48. Su, Chao, Xiaoguang Duan, Jie Miao, Yijun Zhong, Wei Zhou, Shaobin Wang, Zongping Shao (2017) Mixed conducting perovskite materials as superior catalysts for fast aqueous-phase advanced oxidation: a mechanistic study. ACS catalysis 7, no. 1: 388-397. https://doi.org/10.1021/acscatal.6b02303.
49. Lim, Jonghun, Yang Yang, Michael R. Hoffmann (2019) Activation of peroxymonosulfate by oxygen vacancies-enriched cobalt-doped black TiO_2 nanotubes for the removal of organic pollutants. Environmental science & technology 53, no. 12: 6972-6980. https://doi.org/10.1021/acs.est.9b01449.
50. Gayathri, P., T. Akila, G. Alan Sibu, Manickam Selvaraj, Mohammed A. Assiri, V. Balasubramani (2024) Enhancing photovoltaic applications through precipitating agents in ITO/CIS/CeO_2/Al heterojunction solar cell. Inorganic Chemistry Communications 168: 112866. https://doi.org/10.1016/j.inoche.2024.112866.
51. Raman, M. Sethu, J. Chandrasekaran, R. Priya, Murthy Chavali, R. Suresh (2016) Effect of post-growth annealing on the structural, optical and electrical properties of V_2O_5 nanorods and its fabrication, characterization of V_2O_5/p-Si junction diode. Materials Science in Semiconductor Processing 41: 497-507. https://doi.org/10.1016/j.mssp.2015.08.020.
52. Saha, D., R. S. Ajimsha, K. Rajiv, C. Mukherjee, M. Gupta, P. Misra, L. M. Kukreja (2014) Spectroscopic ellipsometry characterization of amorphous and crystalline TiO_2 thin films grown by atomic layer deposition at different temperatures. Applied surface science 315: 116-123. https://doi.org/10.1016/j.apsusc.2014.07.098.

53. Kwon, Oh Hyun, Changheui Jang, Junho Lee, Hu Young Jeong, Young-il Kwon, Jong Hoon Joo, Hongjin Kim (2017) Investigation of the electrical conductivity of sintered monoclinic zirconia (ZrO_2). Ceramics International 43, no. 11: 8236-8245. https://doi.org/10.1016/j.ceramint.2017.03.152.
54. Sasikumar, K., R. Bharathikannan, J. Chandrasekaran, MJJoI Raja (2020) Effect of Organic Additives on the Characteristics of Al/Organic Additive: ZrO_2/p-Si Metal–Insulator-Semiconductor (MIS) Type Schottky Barrier Diodes. Journal of Inorganic and Organometallic Polymers and Materials 30: 564-572. https://doi.org/10.1007/s10904-019-01216-x.
55. Tan, S. O., H. Uslu Tecimer, O. Çiçek, H. Tecimer, Ş. Altındal (2017) Frequency dependent C–V and G/ω–V characteristics on the illumination-induced Au/ZnO/n-GaAs Schottky barrier diodes. Journal of Materials Science: Materials in Electronics 28: 4951-4957. https://doi.org/10.1007/s10854-016-6147-0.
56. Aiswarya, K. U., K. J. Arun, M. D. Aggarwal (2025) Fabrication and Characterisation of high response Cu/(PVA-$CdWO_4$)/p-Si Schottky Diode for Ultraviolet photo Detection. Current Applied Physics. https://doi.org/10.1016/j.cap.2025.09.008.
57. Nawar, Ahmed M., Ahmed M. El-Mahalawy (2020) Heterostructure device based on Brilliant Green nanoparticles–PVA/p-Si interface for analog–digital converting dual-functional sensor applications. Journal of Materials Science: Materials in Electronics 31, no. 4: 3256-3273. https://doi.org/10.1007/s10854-020-02874-1.
58. Al-Ghamdi, Ahmed A., H. Bostancı, Omar A. Al-Hartomy, M. Soylu, Farid El-Tantawy, F. Yakuphanoglu (2014) Preparation of tungsten trioxide nanorods by hydrothermal route: n-tungsten trioxide nanorods/p-silicon p–n junction. Journal of Nanoelectronics and Optoelectronics 9, no. 3: 327-333. https://doi.org/10.1166/jno.2014.1600.
59. Keskin, Bahadir, Cenk Denktaş, Ahmet Altındal, Ulvi Avcıata, Ahmet Gül (2012) Synthesis of Ni (II) porphyrazine peripherally octa-substituted with the 4-tert-butylbenzylthio moiety and electronic properties of the Al/Ni (II) Pz/p-Si Schottky barrier diode. Polyhedron 38, no. 1: 121-125. https://doi.org/10.1016/j.poly.2012.02.033.
60. Ismail, A. M., M. I. Mohammed, S. S. Fouad (2018) Optical and structural properties of polyvinylidene fluoride (PVDF)/reduced graphene oxide (RGO) nanocomposites. Journal of Molecular Structure 1170: 51-59. https://doi.org/10.1016/j.molstruc.2018.05.083.
61. S. Mahato, D. Biswas, L.G. Gerling, C. Voz, J. Puigdollers (2017) Analysis of temperature dependent current-voltage and capacitance-voltage characteristics of an Au/V_2O_5/ n -Si Schottky diode. AIP Adv 7: 085313. https://doi.org/10.1063/ 1.4993553.
62. M. Uma, N. Balaram, P.R. Sekhar Reddy, V. Janardhanam, V. Rajagopal Reddy, H. J. Yun, S.N. Lee, C.J. Choi (2019) Structural, chemical and electrical properties of Au/ La_2O_3/n-GaN MIS junction with a high-k lanthanum oxide insulating layer. J. Electron. Mater 48: 4217–4225. https://doi.org/10.1007/s11664-019- 07193-8.

63. Balaji, M., J. Chandrasekaran, M. Raja, S. Rajesh (2016) Structural, optical and electrical properties of Ru doped MoO_3 thin films and its P–N diode application by JNS pyrolysis technique. Journal of Materials Science: Materials in Electronics 27: 11646-11658. https://doi.org/10.1007/s10854-016-5300-0.
64. Aiswarya, K. U., K. J. Arun, M. D. Aggarwal (2025) Investigations on the current conduction mechanism in PVA-$CdWO_4$ films and the temperature-dependent electrical characteristics of Cu/(PVA-$CdWO_4$)/p-Si metal–polymer–semiconductor diodes. Journal of Physics D: Applied Physics 58, no. 41: 415109. https://doi.org/10.1088/1361-6463/ae0a66.
65. Türüt A B, Bati B, A. Kökçe, Mustafa Sağlam, N. Yalçin (1996) The bias-dependence change of barrier height of Schottky diodes under forward bias by including the series resistance effect. Physica Scripta 53, no. 1: 118. https://doi.org/10.1088/0031-8949/53/1/023.
66. Sibu, G. Alan, V. Balasubramani, Abdullah N. Alodhayb, Muthumareeswaran Muthuramamoorthy, Jayaprakash Kaliyamurthy (2025) Inspection and comparative analysis of light and thermal response dynamics of Cu/V_2O_5/n-Si and Cu/La-V_2O_5/n-Si MIS diodes. Journal of Alloys and Compounds 1010: 177168. https://doi.org/10.1016/j.jallcom.2024.177168.
67. Marnadu, R., J. Chandrasekaran, S. Maruthamuthu, V. Balasubramani, P. Vivek, R. Suresh (2019) Ultra-high photoresponse with superiorly sensitive metal-insulator-semiconductor (MIS) structured diodes for UV photodetector application. Applied Surface Science 480: 308-322. https://doi.org/10.1016/j.apsusc.2019.02.214.
68. Sakthivel, M., S. Stella Mary, V. Balasubramani, Mohd Shkir, H. Elhosiny Ali (2023) Enhanced electrical performance of Ag/Ba–Sn/n-Si/Ag hetero junction diode for photodiode applications. Physica B: Condensed Matter 654: 414692. https://doi.org/10.1016/j.physb.2023.414692.
69. Minami, Tadatsugu, Takashi Yamamoto, Toshihiro Miyata (2000) Highly transparent and conductive rare earth-doped ZnO thin films prepared by magnetron sputtering. Thin Solid Films 366, no. 1-2: 63-68. https://doi.org/10.1016/S0040-6090(00)00731-8.
70. Altowyan, Abeer S., Jabir Hakami, H. Algarni, Mohd Shkir (2023) Enhancing the optoelectronic properties of V_2O_5 thin films through Tb doping for photodetector applications. Journal of Alloys and Compounds 960: 170911. https://doi.org/10.1016/j.jallcom.2023.170911.
71. Abdelrazek, M. M., Ahmed E. Hannora, Rasha M. Kamel, Ibrahim Morad, M. M. El-Desoky (2023) Effect of lanthanum doping on the structure and optical properties of nanocrystalline vanadium pentoxide films prepared by sol–gel method. Optical and Quantum Electronics 55, no. 6: 491. https://doi.org/10.1007/s11082-023-04764-2.
72. Tataroğlu, A. D. E. M., Ş. Altındal (2009) The analysis of the series resistance and interface states of MIS Schottky diodes at high temperatures using I–V characteristics. Journal of Alloys and Compounds 484, no. 1-2: 405-409. https://doi.org/10.1016/j.jallcom.2009.04.119.
73. Altındal, Ş., H. Kanbur, A. D. E. M. Tataroğlu, M. M. Bülbül (2007) The barrier height distribution in identically prepared Al/p-Si Schottky diodes with the native interfacial insulator layer (SiO_2). Physica B: Condensed Matter 399, no. 2: 146-154. https://doi.org/10.1016/j.physb.2007.06.002.

74. Peta, Koteswara Rao, Byung-Guon Park, Sang-Tae Lee, Moon-Deock Kim, Jae-Eung Oh (2012) Temperature-dependent electrical properties of (Pt/Au)/Ga-polarity GaN/Si (111) Schottky diode. Microelectronic engineering 93: 100-104. https://doi.org/10.1016/j.mee.2011.11.019.
75. Dökme, Ilbilge, Şemsettin Altindal (2006) On the intersecting behaviour of experimental forward bias current–voltage (I–V) characteristics of Al/SiO_2/p-Si (MIS) Schottky diodes at low temperatures. Semiconductor science and technology 21, no. 8: 1053. https://doi.org/10.1088/0268-1242/21/8/012.
76. Karataş, Ş., Ş. Altındal, M. Çakar (2005) Current transport in Zn/p-Si (100) Schottky barrier diodes at high temperatures. Physica B: Condensed Matter 357, no. 3-4: 386-397. https://doi.org/10.1016/j.physb.2004.12.003.
77. Tataroğlu, A. D. E. M., Ş. Altındal (2006) Characterization of current–voltage (I–V) and capacitance–voltage–frequency (C–V–f) features of Al/SiO_2/p-Si (MIS) Schottky diodes. Microelectronic engineering 83, no. 3: 582-588. https://doi.org/10.1016/j.mee.2005.12.014.
78. Erdal, Mehmet Okan, Adem Kocyigit, Murat Yıldırım (2019) Temperature dependent current-voltage characteristics of Al/TiO_2/n-Si and Al/Cu: TiO_2/n-Si devices. Materials Science in Semiconductor Processing 103: 104620. https://doi.org/10.1016/j.mssp.2019.104620.
79. Aldemir, D. Ali, M. Benhaliliba, C. E. Benouis (2020) Photodiode based on Al-doped SnO_2: Fabrication, current-voltage and capacitance-conductance-voltage measurements. Optik 222: 165487. https://doi.org/10.1016/j.ijleo.2020.165487.
80. Sze, Simon M., Yiming Li, Kwok K. Ng (2021) Physics of semiconductor devices. John wiley & sons.
81. Neamen, Donald A., Dhrubes Biswas (2011) Semiconductor physics and devices. New York: McGraw-Hill higher education.
82. Vivek, P., J. Chandrasekaran, R. Marnadu, S. Maruthamuthu (2020) Fabrication of Illumination-Dependent Cu/p-Si Schottky Barrier Diodes by Sandwiching MoO_3 Nanoplates as an Interfacial Layer via JNSP Technique. Journal of Electronic Materials 49, no. 7: 4249-4264. https://doi.org/10.1007/s11664-020-08137-3.
83. Su, Guoxiong, Viktor G. Hadjiev, Phillip E. Loya, Jing Zhang, Sidong Lei, Surendra Maharjan, Pei Dong, Pulickel M. Ajayan, Jun Lou, Haibing Peng (2015) Chemical vapor deposition of thin crystals of layered semiconductor SnS_2 for fast photodetection application. Nano letters 15, no. 1: 506-513. https://doi.org/10.1021/nl503857r.
84. Balasubramani, V., J. Chandrasekaran, V. Manikandan, Top Khac Le, R. Marnadu, P. Vivek (2021) Upgraded photosensitivity under the influence of Yb doped on V_2O_5 thin films as an interfacial layer in MIS type Schottky barrier diode as photodiode application. Journal of Solid-State Chemistry 301: 122289. https://doi.org/10.1016/j.jssc.2021.122289.
85. Sil, Sayantan, Arka Dey, Joydeep Datta, Mrinmay Das, Rajkumar Jana, Soumi Halder, Joydeep Dhar, Dirtha Sanyal, Partha Pratim Ray (2018) Analysis of interfaces in Bornite (Cu_5FeS_4) fabricated Schottky diode using impedance spectroscopy method and its photosensitive behavior. Materials Research Bulletin 106: 337-345.

https://doi.org/10.1016/j.materresbull.2018.06.016.

86. Raj, Marnadu, Chandrasekaran Joseph, Maruthamuthu Subramanian, Vivek Perumalsamy, Vijayakumar Elayappan (2020) Superior photoresponse MIS Schottky barrier diodes with nanoporous: Sn–WO_3 films for ultraviolet photodetector application. New Journal of Chemistry 44, no. 19: 7708-7718. https://doi.org/10.1039/D0NJ00101E.
87. Gayathri, P., V. Balasubramani, P. Balraju, M. A. Sayed, Mohd Shkir (2025) Ultra-high photosensitivity response in MIS SBDs enabled by Zn-integrated ZrO_2@ Zn interfacial layers for photovoltaic devices. Physica B: Condensed Matter 417506. https://doi.org/10.1016/j.physb.2025.417506.
88. Balasubramani, V., J. Chandrasekaran, V. Manikandan, R. Marnadu, P. Vivek, P. Balraju (2020) Influence of rare earth doping concentrations on the properties of spin coated V_2O_5 thin films and Cu/Nd-V_2O_5/n-Si Schottky barrier diodes. Inorganic Chemistry Communications 119: 108072. https://doi.org/10.1016/j.inoche.2020.108072.
89. Zu, Baiyi, Bin Lu, Yanan Guo, Tao Xu, Xincun Dou (2014) Simple metal/SiO_2/Si planar photodetector utilizing leakage current flows through a SiO_2 layer. Journal of Materials Chemistry C 2, no. 11: 2045-2050. https://doi.org/10.1039/C3TC32242D.

Supplementary Files

This is a list of supplementary files associated with this preprint. Click to download.

- Table2.docx
- Table2.docx
- Table2.docx
- Table2.docx
- Table3.docx
- Table3.docx
- Table3.docx
- Table3.docx
- Table1.docx
- Table1.docx
- Table1.docx
- Table1.docx
- Table4.docx
- Table4.docx
- Table4.docx
- Table4.docx
- Table5.docx
- Table5.docx
- Table5.docx
- Table5.docx
- Table7.docx
- Table7.docx
- Table7.docx
- Table7.docx
- Table6.docx
- Table6.docx
- Table6.docx
- Table6.docx